Quantifying 3D range of motion using off-the-shelf, low-cost cameras

Nathan Christopher Andrew Jackson

A thesis submitted in partial fulfilment of the requirement of Liverpool John Moores University for the degree of Master of Philosophy

July 2022

Contents

List of figures

List of tables

ABSTRACT

Reliable reconstructions of the joint ranges of motion (ROM) of fossil archosaurs are important in establishing aspects of their appearance, behaviours and palaeoecology. These studies are complicated, however, by the fact that soft tissues, which markedly affect ROM, rarely fossilise. Whilst early reports paid this little attention, there has been a recent shift to using comparisons with the extant phylogenetic bracket of dinosaurs, along with osteological correlates, to account for missing soft tissue in ROM estimates.

The digital revolution in palaeontology has enabled a new insight into these analyses, enabling researchers to conduct range of motion studies freed from the limitations of handling large, heavy and often fragile bones. Advanced workflows such as XROMM (X-ray reconstruction of moving morphology) have enabled the integration of skeletal kinematics and 3D bone models to reconstruct 3D motion in a wide range of species.

Whilst traditionally, methods of digitisation and analysis were prohibitively complicated or expensive, researchers have been working on low-cost, easy-to-use methods of digitisation and analysis in order to widen the scope of these studies and enable them to be used by researchers of all disciplines.

This study presents a low-cost, easy-to-use workflow applying XROMM methods and photogrammetry to an experimental setup involving two off-the-shelf GoPro cameras and easy-to-use software. The workflow's effectiveness is evaluated a) using a LEGO wand with markers placed at a known distance to assess the setup's ability to produce accurate and precise results and b) ascertain the workflow's effectiveness on biological data through the dissection of an ostrich (*Struthio camelus*) foot.

It can be concluded that, whilst the workflow retains XROMM's ability to produce highly accurate and precise results and is potentially effective on biological data, from multiple limitations in the biological data results, it is clear that the workflow is in need of a considerable deal of refinement before it can be considered truly effective.

DECLARATION

No portion of the work referred to in the thesis has been submitted in support of an application for another degree or qualification of this or any other university or other institute of learning.

ACKNOWLEDGEMENTS

1 Introduction

How to estimate range of motion: studies of fossil archosaur limb mobility

The mobility of the limbs of fossil archosaurs, such as non-avian dinosaurs (hereafter "dinosaurs"), is important to reconstructing key aspects of their behaviours, locomotor styles and paleoecology. Range of motion (the full movement potential in any given joint, ROM) in archosaur limbs is an important constraint on reconstructions of limb motion and posture. However, ROM studies (Ostrom and Johnson, 1995; Senter, 2005) have been complicated by the fact that soft tissue, which greatly affects ROM, is generally lost in fossilisation. Muscle scars (Carpenter and Wilson, 2008) and occasional discoveries of calcified articular cartilage (Schwarz, 2007), combined with comparisons with extant functional analogues, provides some insight into the matter, but the role of soft tissue in increasing or decreasing range of motion at any given joint remains an active area of research (Hutson and Hutson 2013, 2014, 2015; Manafzadeh and Padian, 2018).

Another complication in studying the functional morphology of fossilised limbs is that, traditionally, it involved handling very large, potentially fragile bones; however, in recent years, technological advances e.g., laser scanners, photogrammetry, X-ray reconstruction of moving morphology (XROMM) have made it possible for more in-depth studies of functional morphology in the limbs of extinct archosaurs.

The functional morphology of archosaur limbs

The archosaurs (or "ruling reptiles") were the dominant group of vertebrates for most of the Mesozoic era, diversifying over 250 million years and spanning a great variation of body plans, sizes and ecologies. Inevitably, this meant that the group had a great diversity in locomotor habits.

Various aspects of archosaur limb morphology and function – limb support, foot posture, joint structure, and myology – have been subject to a great deal of study by researchers, due to their having important implications for locomotion, behaviour, and paleoecology. Whilst early reports (e.g., von Huene, 1928) were mostly qualitative, there has been a recent and much-needed shift towards rigorous, repeatable experimentation using the extant phylogenetic bracket (crocodylians and birds) as functional analogues for dinosaurs (e.g., Nicholls and Russell, 1985; Bonnan, 2001; Carpenter, 2002; Bonnan and Senter, 2007; Carpenter and Wilson, 2008).

The humeral ROM of the shoulder joint is one area of interest in this regard because this area provides the bony connection between the forelimb and the body wall. One area in which these assessments are vital is information on whether derived theropods (both avian and non-avian) used their forelimbs in terrestrial or aerial locomotion (Bonnan, 2007; Carpenter and Wilson, 2008; Hutson and Hutson, 2013). For example, humeral ROM has been a crucial part of studying the origins of flapping flight in basal birds (Gishlick, 2001), whether pterosaurs used bipedal or quadrupedal locomotion when moving on the ground (Unwin, 1988; Bennett, 1997) and whether large quadrupedal dinosaurs moved their forelimbs in a manner similar to large mammals (Johnson and Ostrom, 1995; Bonnan, 2001; Thompson and Holmes, 2007; Remes, 2007).

A particular area of research is how forelimb ROM affected idiomotion (the use of the limbs in non-locomotory behaviours (Fischer, 1998)) in bipedal dinosaurs, with studies looking at the use of the forelimbs in specific behaviours including prey capture, digging, displays and grooming (Welles, 1984; Nicholls and Russell, 1985; Gishlick, 2001, Carpenter, 2002, Senter, 2005, Senter, 2006, Senter and Parrish, 2006).

Elbow ROM, obtained from fossil specimens, can be compared with extant animals as functional analogues to analyse the possible use of the forelimbs in idiomotion, including prey capture, display and digging (Carpenter and Smith, 2001; Carpenter, 2002; Bonnan, 2003; Senter, 2005; Thompson and Holmes, 2007).

An example of this is White et al (2015), which studied the forelimb ROM in the megaraptoran theropod Australovenator. The study found that Australovenator had a humeral ROM much greater than other large theropods, but similar to that of dromaeosaurids, as well as unguals that were capable of hyperextension. From these results, they theorised that Australovenator primarily used its forelimbs in prey capture – unusually among large theropods.

Studying hip joint ROM has been in important in understanding terrestrial locomotion in archosaurs; in extant archosaurs, the distinctive styles of terrestrial locomotion seen in crocodiles (plantigrade quadrupeds with variably adducted posture) and birds (digitigrade bipeds with fully erect posture) are reflected in their highly disparate hind limb musculoskeletal anatomies. Whilst crocodilians have thick layers of articular soft tissues around their hip joints throughout their lives, mature birds have relatively thin layers of articular soft tissues, (Tsai et al, 2019). The crocodilian condition is of paleobiological importance, since many extinct archosaurs have incongruent, rugose bony joints, like those seen in crocodilians today, with osteological correlates for thick, soft tissue layers on preserved archosaur fossils, such as sauropods (Bonnan, 2004) and large ornithischians (Dilkes, 2001), indicating that, like crocodilians, these structures were important in hip joint function. Fossilised cartilage is sometimes observed at the end of fossil archosaur long bones; however, these structures largely conform to the bone underneath.

The importance of soft tissues in determining functional morphology

Many incorrect interpretations of the appearance and behaviour of prehistoric animals have resulted from not taking the presence of soft tissue into account; a notorious example of this is the inaccurate hypothesis that sauropod dinosaurs were aquatic or amphibious. This theory originated from early observation of the seemingly poorly ossified, "unfinished" ends of sauropod limb bones, which was used as evidence that the limbs were not able to support the body's tremendous weight on land for any extended period of time (Marsh, 1883; Marsh, 1893; Osborn, 1898; Hatcher, 1901). This erroneous notion was held until the 1970s, where further studies, based on anatomical and sedimentological data, found that sauropods were, in fact, fully terrestrial (Bakker, 1971). It was not until 2007 that an articular cartilage capsule was first identified on the distal metaphyses of a sauropod limb joint, when its presence was found on the sauropod *Cetisauriscus* (Schwarz, 2007). Its presence indicated the presence of a large articular capsule on the end of the limb bones of all sauropods, meaning that (based on similar structures found in extant archosaurs) the forelimb length was likely 6-10% longer than had would have been apparent from the bones alone. This is a case study as to how taking epiphyseal cartilage into account can change the way dinosaurs are reconstructed – this discovery revealed that the height to shoulder, and possibly to hip, of sauropod dinosaurs had been previously underestimated, meaning that they were likely taller than had been previously reconstructed.

Another example of erroneous reconstructions resulting from failing to take soft tissue into account is the common practice of reconstructing pterosaurs with abducted hip joints, analogous to those of a bat; this originated from an erroneous 19th century reconstruction of a juvenile *Pterodactylus* (von Sommering, 1817). In recent years, similar hip poses were posited for basal maniraptorans, especially ones associated with four-winged gliding. However, a study that observed the ligamentous constraints of hip mobility in extant birds (Manafzadeh and Padian, 2018), which have similar hip

joints and medially oriented femoral heads to pterosaurs and basal maniraptorans, found that, since the diapsid hip capsule has a ventral ligamentous thickening, it would have been physically impossible for the animal's limbs to assume that pose. From these results, the authors cautioned that reconstructions of joint mobility based on osteological manipulation alone can be misleading.

As Bishop (2021) notes, the absence of soft tissue creates several unknowns in biomechanical studies of fossil vertebrates. The near absence of articular cartilage and other soft tissues raises the question on how accurately preserved joint shapes reflect their shape, spacing and articulation *in vivo*. For this reason, it is important to work out whether the calcified cartilage found on fossil long bones is a good proxy for cartilage *in vivo* – whilst there have been attempts (Bonnan et al, 2010), the overall extent to which articular cartilage covered dinosaur long bones remains frustratingly unexplained. In addition, the absence of articular cartilage leads to concerns on how anatomical and joint co-ordinate systems are determined in 3D motion analysis – the absence of cartilage could affect the skeletal marionette quite markedly. On a related note, there is also limited understanding on how muscle anatomy in extinct species reflects underlying skeletal anatomy – in addition to this, structures such as ligaments, which provide an important contribution to joint control during certain tasks [especially when joint ROM about a given axis is near its limits (Manafzadeh and Padian, 2018)].

Unfortunately, dinosaur skeletons are frequently reconstructed with the ends of the limb bones touching each other, and many functional and biomechanical analyses of dinosaur limb bones also frequently give little to no specific attention to any role played by soft tissues (Parrish, 1986a; Parrish 1986b; Ostrom and Johnson. 1995; Senter, 2005). However, in recent years, there has been a much-needed move towards including estimates of missing soft tissues when framing studies of functional morphology in fossil archosaurs (Suzuki et al, 2010; Hutchinson and Gatesy, 2006; Gatesy et al, 2009; Bishop et al, 2021).

Thulborn (1982) used a correction factor of 9% to hindlimb bone length to account for missing epiphyses when studying speeds and gaits in dinosaur taxa (derived from the bone spacing in a *Thescelosaurus* hindlimb fossil). Hutchinson et al (2005) used correction factors of between 5-10% (7.5% for the femur, 5% for the tibiotarsus and 10% for the metatarsus), extrapolated from modern crocodylians when studying running speed in *Tyrannosaurus*. There is, sadly, still no definitive correction factor on how much epiphyseal cartilage needs to be reconstructed, nor have potential problems associated with ignoring the epiphyseal cartilage been identified. As Holliday et al (2010) note, these are important things to quantify; rather than simply affecting estimations of dinosaur size and height, inferences of epiphysis size may greatly affect our interpretation of joint function, posture, and range of motion in dinosaur limbs.

It is therefore important to investigate whether constraints on the motion of *in vivo* limb joints can be surmised from osteology alone. Fortunately, the extant phylogenetic bracket (EPB) (Witmer and Thomason, 1995), represented by crocodylians and birds, can be used as comparisons for the functional morphology of the limbs of extinct archosaurs. For example, a comparative study of birds and crocodylians (Hutson and Hutson, 2014) was used to determine whether soft tissues contributed to wrist-folding in extant archosaurs, to surmise whether avian-like wrist folding aided locomotion in quadrupedal dinosaurs.

An area of research where comparison with the EPB, combined with osteological correlates of muscle attachment, has revealed information that was not apparent from osteology alone has been the reversions from bipedality to quadrupedality in at least four lineages of non-avian dinosaur (once in sauropodomorphs and three times in different lineages of ornithischian) and the

osteomyological changes associated with its evolution. Traditionally, mostly based on comparisons with large quadrupedal mammals, multiple osteological indicators (e.g. long forelimbs in relation to hindlimbs, elongate trunks relative to hindlimb length, short tails in comparison with trunk length) were used to indicate quadrupedality in various species of ornithischian (e.g. Galton 1970; Thulborn 1977). However, later re-assessment of these indicators, through assessing phylogenetic distributions of the traits, revealed that many of them, for varying reasons, were useless in determining stance (Maidment and Barrett, 2014). From dissection of crocodilian pelvic muscles and the development of thigh muscles in chick embryos, Romer (1927) concluded that features such as the transverse broadening of the ilium and reduced postpubis in some ornithischians were related to the evolution of quadrupedalism, but he did not specify functional causes for those changes. Reconstructing pelvic and forelimb muscles in each major ornithischian clade, Maidment and Barrett (2012) concurred with Romer that significant reorganisation of the pelvic musculature must have taken place in the evolution of quadrupedality – many locomotor muscles on the ilium must have moved laterally and a reduction in the musculature originating on the pubis likely took place, resulting in significant changes to muscle moment arms and therefore muscle function. Whilst studies into the limb morphology of quadrupedal ornithischians have revealed a suite of osteological and myological changes associated with quadrupedality, these characteristics were acquired convergently at different times and had different functions. For instance, the scapulae of both ankylosaurs and hadrosaurs have a laterally projecting acromial process but each used their forelimbs in very different ways during locomotion (Maidment and Barrett 2012). Biomechanical approaches and reconstruction of soft tissue using the EPB revealed that ornithischian dinosaurs displayed an array of locomotor styles that skeletal convergence only partially predicts. This underscores the need to consider additional information from reconstruction of soft tissue characteristics when determining the functional morphology of extinct taxa, as skeletal morphology alone may not be a particularly useful predictor of function (Maidment and Barrett, 2012).

The distinctive terrestrial locomotor styles of birds (digitigrade bipeds with a fully erect posture) and crocodiles (plantigrade quadrupeds with variably adducted posture), mean that they have highly disparate musculoskeletal anatomies, especially in the limbs. For example, the avian hip joint has relatively thin layers of articular soft tissues (Rubenson et al, 2007), whilst the crocodilian hip joint retains thick layers of articular soft tissues throughout life (Holliday et al, 2010). Since osteological correlates argue for thick layers of articular soft tissue in extinct archosaurs, as seen in psuedosuchians (Nesbitt et al, 2009), sauropods (Bonnan et al, 2001) and large ornithischians (Dilkes, 2001), the crocodilian condition is likely the ancestral one for both bird- and crocodile-line archosaurs, which modern birds have lost.

Whilst both birds and crocodylians can be used as extant analogues, crocodylians (more specifically, the American alligator) are generally preferred as a model for limb joint ROM in fossil archosaurs. This is largely because crocodylians have joint morphologies more typical of the vast majority of fossil archosaurs (Hutson and Hutson, 2012; Tsai et al, 2019) rather than the more derived joints that are seen in birds. Based on inferred muscle position from observation of muscle scars on fossil shoulder joints and osteological correlates on fossilised hip joints (Tsai et al, 2019), the soft tissues surrounding the shoulder and hip joints of non-avian dinosaurs were probably more similar to crocodylians than those of extant birds (Carpenter and Wilson, 2008; Tsai et al, 2019). Conversely, birds (both flight capable and flightless) are rarely used as analogies for ROM in the elbow and shoulder joints of extinct non-avian archosaurs, due to their highly derived elbow and shoulder morphologies (Hutson and Hutson, 2013).

The effects of soft tissue on range of motion

One question when studying the functional morphology of fossil archosaur limbs is whether the presence of soft tissue increased or decreased the range of motion of any given joint. Figuring this out is important for extrapolating the *in vivo* ranges of motion in fossil archosaurs. However, this remains a rather contentious subject, as using differing extant analogues to study the range of motion present at any given joint can lead to conflicting results – a good example of this is the ongoing debate of the *in vivo* posture, elevation, and flexibility of the necks of sauropodomorph dinosaurs.

Early works described sauropod necks as extremely mobile (Marsh, 1883; Hatcher, 1901), with avian-like flexibility; however, in the late 1980s, John Martin, based on mounting the skeleton of the Middle Jurassic sauropod *Cetiosaurus*, proposed that sauropod necks were likely largely inflexible (Martin, 1987). This was further corroborated by studies using computer models of the sauropods *Apatosaurus* and *Diplodocus* in the 1990s stated that the necks of these sauropods were likely very inflexible (Stevens and Parrish, 1999), with *Diplodocus* being barely able to raise its neck above the horizontal.

Dzemski and Christian (2007), by measuring ROM in ostrich neck vertebrae at different levels of dissection to analyse how soft tissues might have affected the *in vivo* ROM of sauropodomorph neck vertebrae, observed that the presence of soft tissues restricted the neck's ROM to a minor degree. These results were corroborated by Cobley et al (2013) who found that the presence of soft tissues and cartilage most likely limited ROM beyond the limits beyond what simply observing the osteology of the neck vertebrae would suggest, implying that sauropod necks were largely inflexible.

However, Stevens and Parrish (1999)'s results have been questioned by some researchers (Taylor and Wedel, 2013) on the grounds of a) setting arbitrary zygapophyseal safety limits (50%) for disarticulation, when there was no evidence that this was true of the bones, and later studies found that the zygapophyseal overlap was likely far less than Stevens and Parrish's figures and b) underestimating the role of intervertebral and zygapophyseal soft tissue/cartilage in the range of motion of the sauropodomorph neck.

Using CT scans of fossils and the cartilage:bone ratio of extant birds to extrapolate the likely anteroposterior length of sauropod zygapophyseal facets when cartilage was added to them, Taylor and Wedel (2013) found that including cartilage in sauropod neck reconstructions increased the dorsoventral flexibility at each joint in the neck vertebrae; increasing the length, elevation, and overall flexibility of sauropod necks *in vivo*. Taylor (2014) further observed that bone morphology alone is not necessarily an indicator of *in vivo* range of motion and noted that the differing effects of intervertebral cartilage on neck flexibility across taxa would be a worthy area of study.

Another potential complication with extant analogues is that, in analogous structures, ROM may be affected in different ways. Vidal et al (2020), studying the basal eusauropod *Spinophorosaurus* and comparing it to extant giraffes, found that, whilst the two had a similar total neck range of motion, the giraffe had greater intervertebral flexibility; the sauropod achieved the same range of motion as the giraffe by having a greater number of cervical vertebrae. They also concluded, contrary to Taylor and Wedel's (2013) assertations, bone articulation in the osteologically neutral pose can be used to estimate intervertebral space accurately and that disarticulation of the cervical vertebrae is not required to attain extreme neck postures.

Vidal et al (2020) also noted that many sauropods, unlike giraffes, possessed long, ossified, overlapping cervical ribs, which have been theorised to have been ossified tendons (Klein et al,

2012). The presence of these cervical ribs have been used as evidence for immobile necks in sauropods (Martin et al, 1998) and other tetrapods (Tschanz, 1988). However, similar structures in the tails of dromaeosaurid theropods seem to allow for considerable motion of the tail; whilst the presence of these did affect ROM, it was likely far less than previously assumed.

Whilst some reports in the literature (e.g. Yalden, 1966; Shubin et al, 2006) claim that some types of soft tissue act to increase the range of motion at limb joints, because of enlarged articular cartilage in comparison to the corresponding body tissue, others have raised concerns that the articular cartilage of archosaurs does not faithfully represent the articular morphology of the bone underneath (Holliday et al, 2001). For example, crocodilians have thick layers of articular soft tissues in their hip joints and epiphyses throughout life, and the shape and size of the articular surfaces differs significantly from the bony morphology underneath, unlike what is seen in therian mammals and mature birds, which have relatively thin layers of articular soft tissues, which match the bone morphologies underneath (Tsai et al, 2019). Birds also have more strongly defined distal condyles in the femur and more intra-articular structures than those of crocodiles (Manafzadeh and Padian, 2018).

Solving this debate will have important implications for our ability to infer joint morphology, posture, and locomotor styles in many fossil archosaurs – and for different joints, the answer varies. For instance, some studies have confirmed that articular surfaces of the bones within the elbow joints do indeed provide a general approximation of mobility (Hutson and Hutson, 2012) in extant archosaurs, indicating that these can be used as a reliable indicator of ROM in fossil ones. However, Tsai et al (2018) observed that many extinct archosaurs had highly incongruent hip joints, based on both comparisons with extant crocodylians and osteological correlates for thick layers of articular soft tissue on fossilised archosaur hip joints.

Since the absence of articular cartilage in fossilised limb bones and the role articular cartilage plays in range of motion *in vivo* is rarely considered, many reported fossil ROMs of the joints in dinosaur limbs likely greatly underestimate the actual *in vivo* ROM; this is especially true if the bony limb elements were moved to the point of disarticulation.

Whilst a general knowledge of the effect that soft tissue has on individual joint thickness and range of motion in archosaurs would be useful, this is rarely quantified (Bonnan et al, 2010; Dzemski and Christian, 2007). This means that it is often debated whether soft tissue restricts or increases the range of motion *in vivo* at any particular joint. In a similar vein, it has been debated whether the articular surfaces of fossil archosaur bones accurately reflect cartilage morphology *in vivo* (Holliday et al, 2001: Hutson and Hutson, 2012). Sadly, many investigators acknowledge that the methods that they have used are not conducive to repeatability and rarely mention statistically analysing data, making their empirical validity questionable at best. However, despite these pitfalls, the practice of manipulating fossil archosaur limbs to obtain ROM is a growing area of interest.

A problem of studying the ROM of archosaur limbs (as outlined by Hutson and Hutson, 2012) is that, rather than using dead specimens at varying stages of dissection (as is commonly done in such studies), the voluntary ROM of joints should be measured *in vivo*. Whilst a possible way to do this would be to immobilise the limb of a living research subject and record its voluntary joint ROMs over time, this would prove both risky and impractical with large, aggressive, and potentially dangerous research subjects (e.g., adult ostriches). Hutson and Hutson (2012) propose, as an alternative, that *in vivo* ROMs could be measured using digital inclinometers strapped directly to the limbs of anaesthetised or freshly dead specimens, allowing the ROM to be isolated by electrically stimulating relevant muscles or muscle groups or by recording a range of voluntary ROMs from the specimens

over time. The data could then be relayed to a computer and statistically analysed, before being compared with a skeletonised ROM of the same limb segments.

The digital revolution; digitisation in palaeontology

Palaeontology has been revolutionised in recent years by using powerful methods for the digital visualisation and analysis of fossil material. These include radical improvements and increased availability in computer technology, and in tomographic techniques, enabling 3D reconstructions of specimens to be made (Cunningham et al, 2014). These new imaging techniques allow for poorly understood or unknown anatomical details of fossil taxa, as well as microfossils or trace fossils to be described in much greater detail.

Digital methods have enabled multiple major advances in palaeontology. Structures that were near-impossible to visualise can now be observed as never before (Gauthier et al, 2012). In some cases, this has allowed inferences of behaviour to be made – as an example, from virtual endocasts of vertebrate braincases, inferences can be made about sensory and locomotory capabilities of extinct taxa (Alonso et al, 2004; Lautenschlager et al, 2012).

CT scans can be used to study the developmental sequence of fossil organisms by observing the preserved growth lines within the mineralised skeleton of the adult specimens without destructive histological sampling. This approach has been used for taxa ranging from protists (Schmidt et al, 2012) to invertebrates (Murdock et al, 2012) and vertebrates (Rucklin et al, 2012), extracting the juvenile morphologies preserved within the adult skeleton.

Digitisation, and the use of 3D digital models, has become particularly important in analyses of the functional morphology of fossil organisms, with the tools used for recreating and analysing anatomical structures becoming more and more powerful and easier to use. This has enabled previously untestable hypotheses, such as finite-element analysis of stress and strain (e.g., Rayfield, 2007) or hydrodynamic modelling (e.g., Shiino et al, 2009; Troelsen et al, 2019), to be tested without fear of damaging a potentially fragile specimen. Furthermore, many fossil species have been characterised in this manner, allowing for comparative analyses and evolutionary trends to be revealed.

In tandem with this, the digitisation of skeletons has enabled researchers to analyse musculoskeletal functions and aspects of biomechanics in extinct animals (Falkingham, 2012; Gatesy et al, 2022), such as skeletal kinematics and 3D joint ranges of motion. The advantages of 3D modelling are numerous – they remove the limitations of having to handle large, heavy and often surprisingly fragile bones; they require only a computer to work with, making them more convenient to study, parts of the specimen can be isolated without risk of damage and digitisation allows for specific elements to be marked, making interpretation easier.

By digitising skeletons or limbs, constraints and forces can also be applied to the digital models that allow simulations that would be impossible if relying on specimens alone (e.g., Rayfield, 2007), as well as accurate 3D surfaces allowing for more specific placements of muscle attachments than would be possible with generic computer models.

The proliferation of digital datasets also allows 3D data to be shared and disseminated, providing a possible solution when fossil material is rare or inaccessible, allowing for further collaborative analysis; in some cases, it can even be used to safeguard valuable specimens. In principle, this can provide palaeontology with a sense of openness that other biological sciences have.

In conclusion, digitisation is transforming the way that fossils are studied and providing greater insight into the paleobiology of extinct groups and theories for them (Cunningham et al, 2014). It would be no exaggeration to say that digitisation has revolutionised the field of palaeontology; enabling the implementation of new methods that enhance our understanding of the history of life in a way that was previously nigh-impossible.

Digitisation Methods

Digitisation of specimens is generally done in three different ways; laser scanning or photogrammetry, which both capture external geometry, and CT scanning, which records internal geometry too.

Whilst Laser scanners come in a variety of models, they are generally suited to a specific range and object size – for instance, a desktop scanner generally lacks the range to scan large specimens or field sites. Whilst scanners are gradually becoming more affordable as their use becomes more prevalent, few palaeontology research groups own their own scanners, instead having to acquire them through either rental or borrowing. Once data has been acquired, proprietary software and/or a high level of expertise is necessary to both align the individual scans and clean spurious data.

In photogrammetry, overlapping photographs of an object taken with a digital camera are used to create a 3-D digital model. Compared to laser scanning, photogrammetry is more accessible, only requiring access to a camera and a computer – due to this, over the last decade, photogrammetry has become common in palaeontology, and has been used to digitise a wide range of specimens, from dinosaur trackways (Falkingham et al, 2021; Lockley et al, 2021) to large, mounted specimens (Romano et al, 2021).

The first step is to acquire photographs of the specimen. The number of photographs varies according to both the specimen's complexity and to the resolution required of the digital model; from as little as three photographs for less complex specimens, to up to several thousand for complex specimens. However, to produce a three-dimensional coordinate, any given point must be present in at least three photographs from different positions.

After having acquired an image set of the specimen, the next step is to calculate camera positions to create a 3D object – this can be done using open-source software. The production of the initial 3D surface from photographs or surface scans is largely automated, with the most critical data being the finished 3D surface files. Colour data from the surface can also provide useful information and this should be included if available.

A text file of metadata is also required to document the imaging settings and techniques used to generate the 3D model. The preparation of this may involve a range of operations, including trimming irrelevant data, the fusion of the components into a single mesh, and smoothing, hole filling and/or manual manipulation of the location of individual point coordinates or surfaces; these all should be detailed.

The original capture data allows for verification of the processes used to generate the model and should be included. Whilst for 3D scanning, it may only be possible to release the data in a proprietary format, compatible surfaces should be exported where possible. For digital alignment of different aspects or manual intervention in model construction, unfused data should be released as accuracy of original alignment may vary in quality.

Unlike laser scanning, photogrammetry relies on contrast differences to produce points; because of this, areas of solid colour will not result in points within the point cloud. Whilst this does help in

removing unwanted areas, it can cause difficulties for objects such as scale bars; however, since solid colour only occurs on flat surfaces, no information is lost. A potential pitfall of the method is that the resulting point-cloud is scale-less. To fix this issue, an object of known dimensions should be included; this will aid in scaling the point cloud to the correct dimensions. Difficulties also arise when attempting to produce models of specimens or outcrops in complex surroundings (Falkingham, 2012). In cases where the background is complex in colour and topology or when it appears in many photographs, a large portion of the point cloud may represent extraneous and unwanted parts; whilst these can be removed, doing so increases both processing and post-processing time. This problem can be averted by placing small specimens on a plain background, whilst, for larger specimens, the depth of field of the photograph must be focused on the specimen (ideally, the specimen should be mounted against a wall or floor).

The digitisation of palaeontological resources represents an exciting advance for paleontological science, and the adoption of this method will greatly facilitate research, allowing workers in all areas access to technology that has previously remained prohibitively complicated and expensive. The widespread adoption of 3D digitisation, once associated pitfalls are overcome, will also aid in collaboration through the sharing and dissemination of digital data.

XROMM and XMALab

Traditionally, most studies of skeletal kinematics came from motion capture of external markers attached to skin or tight clothing. However, these estimates suffered due to a poor fidelity of skin movement to underlying bone movement, decreasing the reliability of data analysis (Filipe et al, 2006). In addition, these methods were restricted to measuring the motion of structures at or close to the skin surface and were unable to visualise deep internal structures (e.g. the spine).

XROMM (X-ray reconstruction of moving morphology) is a set of 3D X-ray motion analysis techniques for combining skeletal morphology data from a CT scan with bone motion data from *in vivo* X-ray videos (Brainerd et al, 2010, Gatesy et al 2010); with the result being a precise and accurate animation of 3D bone meshes moving in 3D space. Researchers have used XROMM to study *in vivo* skeletal motion in numerous species, including terrestrial locomotion in alligators (Baier and Gatesy, 2013) and birds (Kambic et al, 2014, 2015), flight in birds (Baier et al, 2012; Heers et al, 2016), forelimb kinematics in rats in order to serve as a proxy for Mesozoic eutherians (Bonnan et al, 2016), trackway formation in theropod dinosaurs (Falkingham and Gatesy, 2014, Turner et al 2019, 2020), and musculoskeletal linkages (Camp and Brainerd, 2015) and cranial kinematics (Olsen et al, 2017; Camp et al 2020; Camp and Brainerd 2022) in suction-feeding fish. Of particular relevance to this dissertation, XROMM has been increasingly used to explore range of motion, both *in vivo* and in cadaveric specimens (Kambic et al, 2014; Manafzadeh and Paidan, 2018

XROMM methods include marker-based XROMM (Brainerd et al, 2010), in which radio-opaque markers are surgically implanted into skeletal elements and markerless XROMM, which includes manual alignment of bone models to video sequences (e.g. scientific rotoscoping) (Gatesy et al, 2010) and semi-automated bone model registration methods (Banks and Hodge, 1996; Miranda et al, 2011). Implantation of radio-opaque bone markers allows bone models to be animated directly from bone marker coordinates, offering potentially higher throughput and more precise results, but at the expense of requiring invasive surgery.

Previously, XROMM required specialised software for the correction of distortion introduced by fluoroscopic image intensifiers, calibrating cameras, tracking radio-opaque markers and calculating rigid body motion (Brainerd et al, 2010). It also resulted in complex file management: at least seven

16

files as inputs, which then produced 22 files as outputs; this means a total of 29 files per trial and 725 files for small studies with 25 trials, (for more on this, see Brainerd, 2017).

However, new open-source software packages have been made (and continue to be developed) to account for these issues; XMALab and XMAPortal (Knorlein et al, 2016). XMALab (X-ray motion analysis lab), whilst designed for XROMM, works equally well for motion analysis from standard video cameras. It is also fully open-source and does not require proprietary software to run, whilst XMAPortal (xmaportal.org), manages calibration images and X-ray video files and stores the original x-ray video data with its essential metadata. XMAPortal, in order to counteract the problem of file management associated with XROMM, is an open-source, online database made to manage calibration images and X-ray videos.

XMALab, and the XROMM workflow will be fundamental to the work carried out in this thesis, facilitating an open, easy to use workflow for 3D marker tracking.

Conclusion

Digitisation has revolutionised the study of functional morphology in fossil organisms, allowing researchers to investigate ranges of motion, constrain soft tissue values and explore aspects of biomechanics in extinct animals, free of the limitations that arise having to handle large, heavy and often surprisingly fragile bones. This allows previously untestable hypotheses to be adequately tested. By digitising skeletons or limbs, constraints and forces can also be applied to the digital models that allow simulations that would be impossible previously, as well as accurate 3D surfaces allowing for more specific placements of muscle attachments than would be possible with generic computer models.

Advanced workflows such as XROMM can be used to combine skeletal morphology data and bone motion data to create accurate 3D models of bones moving in 3D space, allowing for *in vivo* locomotion to be studied in various species.

Despite the obvious advantages of digitisation of specimens, however, the constraints of excessive cost (in the case of laser scanning), the use of large and cumbersome X-ray machines and laser scanners and a high level of required expertise (in the case of photogrammetry) has rendered the means to do so largely inaccessible. In a similar vein, XROMM is constrained by requiring specialised proprietary software and complicated file management, making it cumbersome to operate, especially for new users.

However, there are researchers working on methods to reduce these costs, creating low-cost, easy-to-use methods of digitisation and analysis; photogrammetric methods exist that can be done using free, open-source software and photos taken by a cheap consumer camera. This, combined with open-source software programmes that do not require cumbersome proprietary software to run such as XMALab, will allow researchers from any discipline access to methods of analysis that previously were prohibitively complicated and expensive.

This aim of this study is to adapt the XROMM/VROMM workflow by collecting video data using two comparatively inexpensive Go-Pro cameras, and creating digital models via photogrammetry, potentially expanding the accessibility of the workflow for researchers of all disciplines.

The following chapters will demonstrate an attempt to apply the XROMM workflow, via the open-source XMALab, to light-video data recorded with affordable, off-the shelf cameras, in order to record range of motion in cadaveric material. Chapter 2 will introduce the experimental setup. Chapter 3 documents accuracy and precision of the methods, and how that varies with differing

camera parameters and variations of experimental setup. This workflow will then be applied to a progressive dissection of an Ostrich foot in Chapter 4. Finally, the work will be summarised and discussed in Chapter 5.

2 Experimental set-up and workflow

Introduction

For this study, I will be assessing a low-cost, easy-to-use workflow that applies XROMM methods to motion data from standard light-video cameras. The application of XROMM methods to footage from light-video cameras is called video reconstruction of moving morphology (VROMM), which has previously paired high-speed videography with 3D models (Brainerd and Laurence-Chasen, 2015). Whilst this method is relatively new, it has been used to measure neurocranial kinematics in suction-feeding fish (Jimenez et al, 2018) and pectoral fin movements during yaw turns in Pacific spiny dogfish (Hoffmann et al, 2019).

Two GoPro Hero 7 Black cameras were placed at 45 degrees from each other and were calibrated using a calibration object made out of LEGO bricks in order to calculate the parameters for both cameras. Once the videos had been taken, they were synchronised manually using the video-editing software in Blender and exported into XMALab, where the individual markers were tracked, and rigid body transformations (RBTs) computed. The specimens used were then digitised using photogrammetry. Finally, the rigid body transformations computed in XMALab were used to animate the 3D models in Autodesk Maya.

In order to ascertain the accuracy and precision of the setup, a LEGO wand, with six markers placed on it at known distances, was moved by hand and recorded by the GoPro cameras with various resolution and framerate settings (Chapter 3). The results of this work determined optimal parameters for a biological case study (Chapter 4).

Experimental Setup

Video Capture

To collect video data, two GoPro Hero 7 Black cameras, placed at ~45 degrees to each other, were used. GoPros were chosen because they are comparatively inexpensive (£270 each), easy to use and offer a high picture quality at a wide range of resolutions (up to 4k), fields of view (linear, wide-angle, and super-view) and framerates [up to 240 frames per second (fps)]. This gives them a greater degree of versatility than many other cameras. In addition, due to being rather small and compact, they are easy to transport, store, and position. To maintain consistent light levels, an LED ring light on a tripod was used. (For more detail on the setup, see next chapter).

Synchronisation

The GoPros were remotely triggered, either using a Wi-Fi remote or through voice commands. This method of triggering is not perfectly synchronous. When triggered simultaneously, one of the cameras would start recording slightly later than the other (roughly 2-4 frames or between 33-66 milliseconds), necessitating synchronisation to be done manually after capture.

A Samsung mobile phone stopwatch was used to ensure that the cameras were fully synchronised. A potential pitfall of using this is that the mobile phone's screen refresh rate was 60fps (with a temporal resolution of 0.016 seconds), meaning that its use is less effective at higher framerates due to a risk of the camera "overtaking the phone" (the phone stopwatch may be static for 2-4 frames of the video footage).

To manually synchronize the footage taken, the open-source computer graphics software Blender v2.91 (www.blender.org) was used. The individual videos from each camera were temporally aligned

such that the time shown on the stopwatch was identical in both videos, throughout the timeline. Video was then trimmed, exported, and loaded into XMALab.

Calibration

Camera calibration is required to calculate 3D co-ordinates of the markers from the 2D points tracked in each video. Starting with images of an object with known dimensions, the process generates a mathematical model of camera position and orientation in 3D space, as well as the camera's internal parameters (Knörlein et al. 2016).
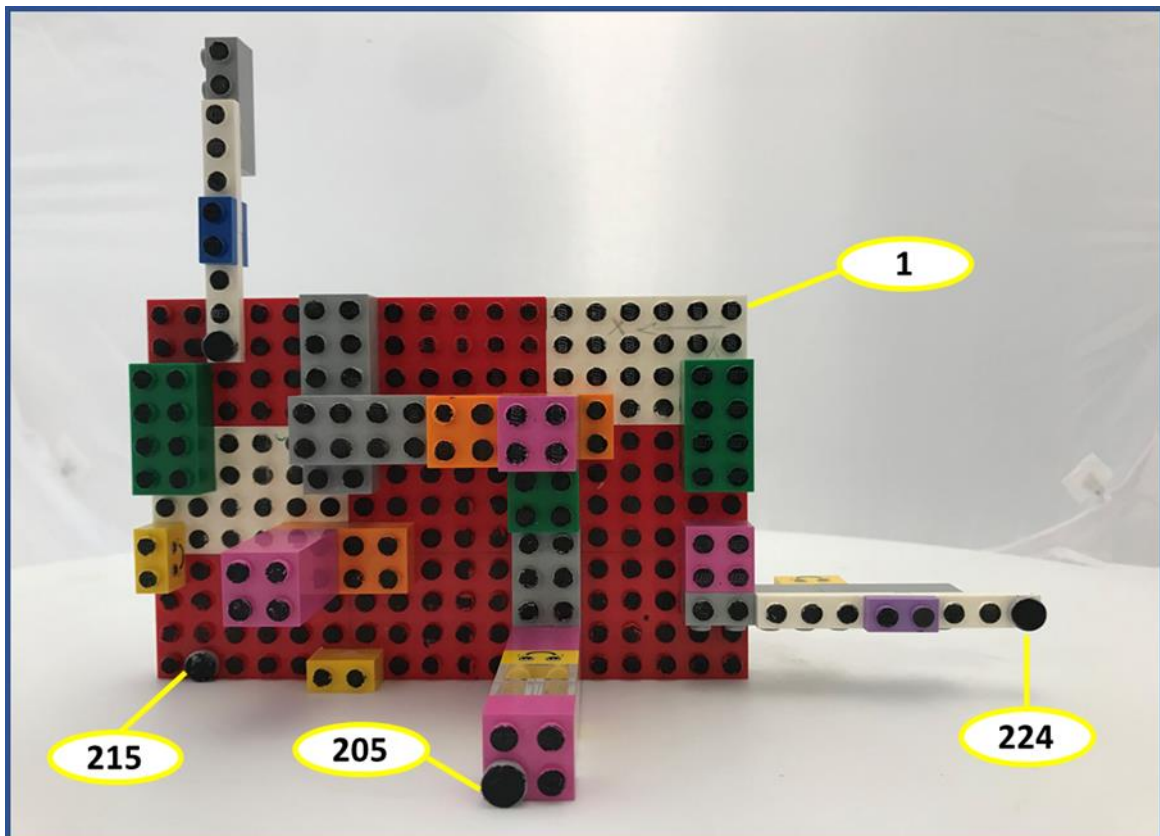
Figure 2.1 - The calibration object - reference markers (markers 1, 205, 215 and 224) labelled.

Camera calibration was carried out using a calibration object (dimensions 184mm by 32mm) constructed out of LEGO blocks, with XYZ co-ordinates of each raised nub entered into a CSV file based on known LEGO dimensions. Four specific nubs (markers 1, 205, 215 and 224) were chosen as reference points (see figure 2.1) and a separate .ref file created with this information. The reason why LEGO bricks were used to construct the calibration object is because LEGO bricks are manufactured with a high degree of precision (tolerance 0.002mm), since they must fit together firmly and yet be easily disassembled (see Knorlein et al, 2016).

The calibration object has smaller bricks placed irregularly on top of it to extend the object into three dimensions, with extra bits reaching out from the top and right sides in order to maximise coverage of the image. The nubs on the calibration object were painted black to enable them to stand out and be automatically recognised by XMALab.

Marker tracking

XMALab (X-ray motion analysis lab) (Knörlein et al. 2016), whilst designed for XROMM, works equally well for motion analysis from standard light-video cameras. The XMALab user interface contains three workspaces: Undistortion, Calibration (see figure 2.2a) and Marker tracking (see figure 2.2b).

Since VROMM uses data from video cameras, rather than X-ray cameras, the footage taken here lacked the complex image distortion seen in fluoroscopic videos. Whilst GoPros semi-automatically undistort video footage, at the wide and super-view fields of view, this may not be perfect (see figure 2.2). As part of the calibration setup, XMALab uses a standard camera distortion model.
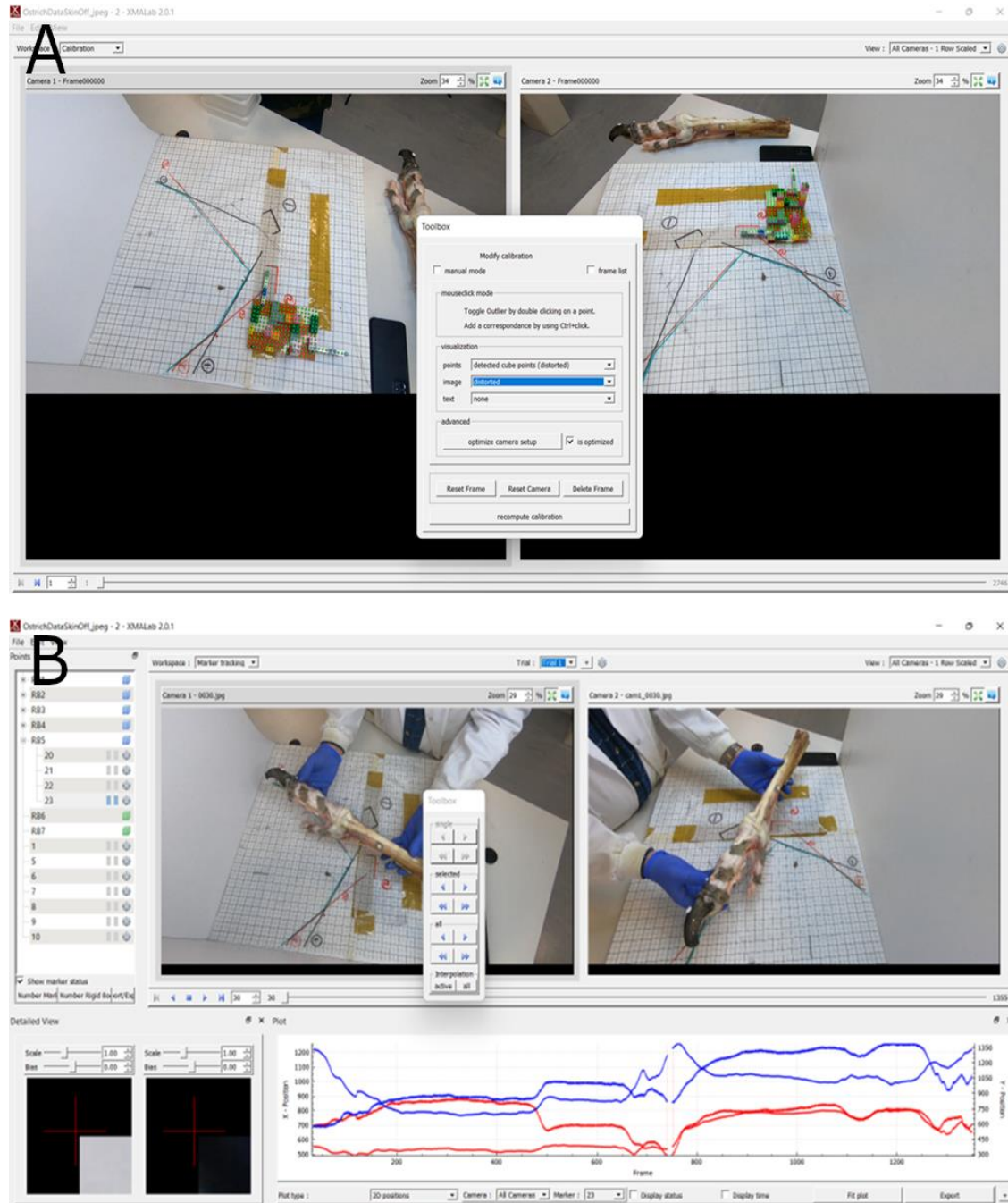
Figure 2.2 – Workspaces in XMALab. A) Calibration. B) Marker tracking. Points window (top left). Main video and automated point tracking window (top centre and right). Detailed View enabling manual refinement of tracking (bottom left). Plot window showing 2D positions (bottom centre and right). (Four other plot types are available)

In the Calibration workspace, users load one or more sets of calibration images for two or more cameras, along with a frame specification file containing the XYZ co-ordinates of all positions on the object. The user identifies four locations on the 3D object, XMALab then detects all visible calibration points and provides the user with feedback on goodness of fit (error) of detected points relative to the object's known geometry. The user can then manually include or exclude calibration points and refine the locations of points if required.

The Marker tracking workspace (see figure 2.2b) provides a Toolbox for automatically tracking points. Specific points can be named and selected in the Points window. For each point, users can select the type of automatic detection (X-ray marker, black marker, white marker, blob detection, etc). Selecting a point makes it active in the Camera views, Detailed View window and Plot window. The Points (see fig 2.2b) window is also used to group sets of markers located in the individual bones into rigid bodies. Points can be set, moved, or selected with the left mouse button and modifier keys, the mouse wheel zooms the cursor position, and the right mouse is used for panning.

The Detailed View (see figure 2.2b, bottom left) window shows a magnified view of the selected point and permits manual refinement of its position. Manual refinement is often necessary when automatic tracking fails, particularly when radio-opaque markers either intersect or overlap with other radio-opaque objects in the scene. The Plot window (see figure 2.3) offers six different viewing options: 2D positions, 3D positions, marker to marker distance, reprojection error, rigid body transformations and rigid body error. Clicking on a frame in the plot window moves the Camera view and Detailed View windows to that frame, and shift-dragging over data and pressing the delete key removes tracked points. The Plot window updates automatically as points are tracked, providing instant feedback on tracking, as well as updating if the user goes back to fine-tune the undistortion or calibration.

Erroneous point positions can be identified in the reprojection error plot (see figure 2.4d), which shows the mean error in pixels of the calculated 3D point reprojected back onto the 2D image planes. In addition, errors can also be detected in the marker-to-marker distance plot of the distance between a pair of markers. Since distances should be constant for markers implanted in the same skeletal element, co-osseous points with particularly large deviations likely reflect poorly tracked frames.
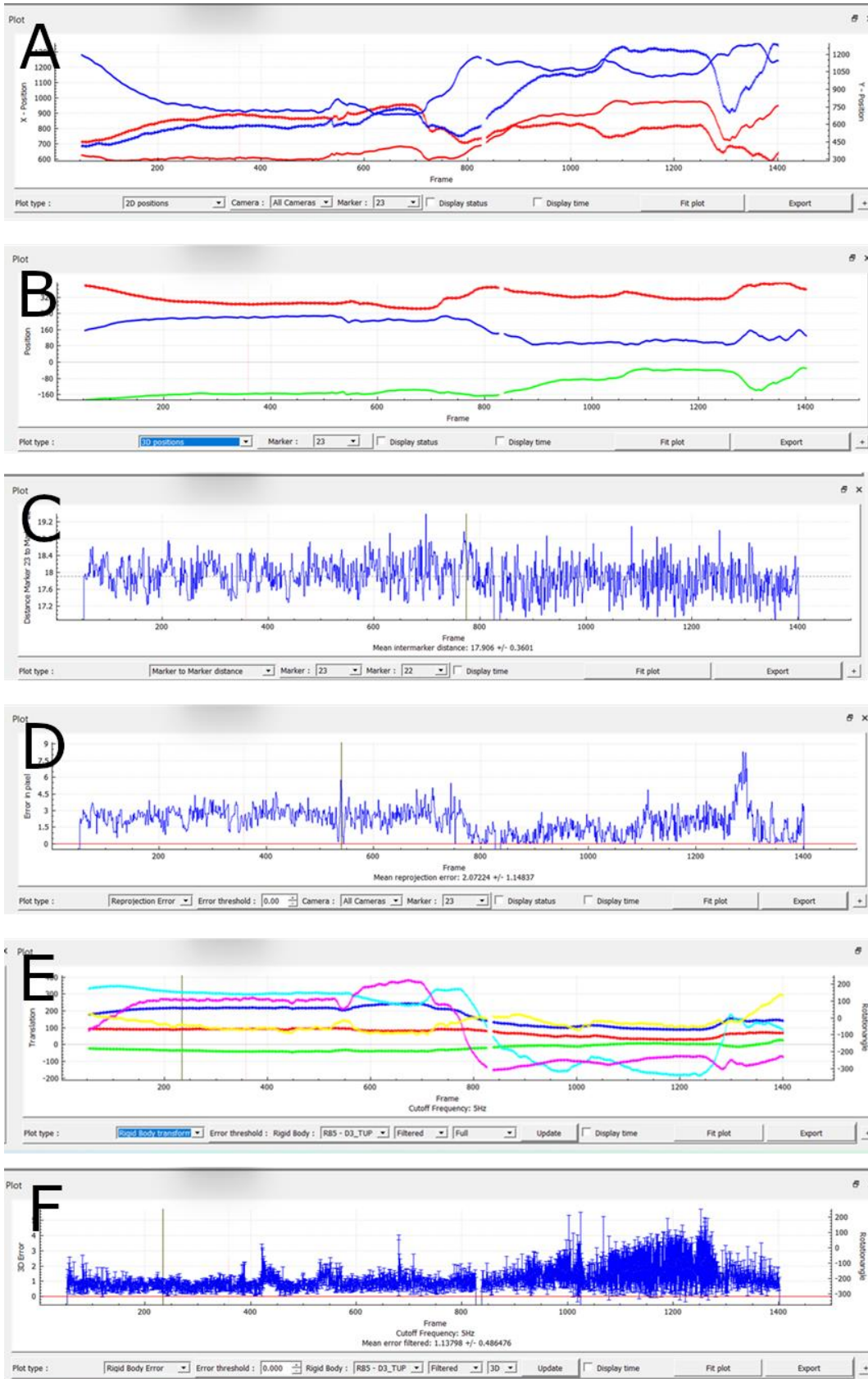
Figure 2.3 - The Plot window. A) 2D positions, B) 3D positions, C) Marker to marker distance, D) Reprojection error, E) Rigid body transformations and F) Rigid body error

Photogrammetry

In photogrammetry, photographs are aligned, and the camera's positions calculated, enabling production of a 3D digital model (Falkingham, 2012; Mallison and Wings 2014). Over the last decade, photogrammetry has become commonly used as a digitisation tool in palaeontology, particularly on dinosaur tracks (Falkingham et al, 2021; Lockley et al, 2021) and large mounted specimens (Romano et al, 2021). It has also become useful in studies of extant taxa, being used to help assess topics from body axis scaling in burrowing skinks (Irschick et al, 2020) and assessing body mass in whales (Irschick et al, 2019). Photogrammetric workflows exist (Falkingham et al, 2012; Mallison and Wings, 2014) that require little user expertise and can produce highly accurate 3D digital models using only photographs taken from a consumer camera and freely available online software.

The first step is to acquire photographs of the specimen – the number of photographs needed vary according to both the specimen's complexity and to the resolution required of the digital model. However, to produce a three-dimensional coordinate, any given point must be present in at least three photographs from different positions. After having acquired an image set of the specimen, the next step is to calculate camera positions to create a 3D object. For the purposes of this study, the imaging software Agisoft Metashape was used – Metashape was chosen because of its ability to reliably produce highly accurate and detailed 3D models, whilst being relatively inexpensive ($59 for an academic license), not requiring an Nvidia graphics card to function, and its easy-to-learn intuitive interface. Open-source alternatives exist (Falkingham 2012, see also e.g. Alicevision Meshroom, COLMAP), but the stringent hardware requirements (i.e. reliance on Nvidia GPUs) and often less-streamlined workflows makes them slightly harder to use here.

After the photos are loaded into Metashape, they need to be aligned. During this stage, Metashape searches for common points on photographs and matches them – in addition to finding the position of the camera for each picture and refining camera calibration parameters, forming a sparse point cloud and a set of camera positions. These can be inspected and incorrectly positioned photos can be removed. The accuracy of the alignment procedure can be altered – whilst higher accuracy settings help to obtain more accurate position estimates, they also increase processing time. This can be sped up by enabling image pair preselection, which selects a subset of image pairs and matches them. The upper limit of key points (points on a 2D photograph that the program deems to be an important feature) and matching points (common points that appear in multiple photos) on every image can also be adjusted – whilst using zero value allows Metashape to find as many key points as possible, it may also be less reliable.

Based on the estimated camera positions, Metashape calculates the depth information for each image. Multiple reconstruction parameters can be specified at this stage. For example, the reconstruction quality can be specified – higher-quality settings create more accurate and detailed models, but also have longer processing times. Metashape then creates a 3D mesh. A texture for the model can be built to add colour information – colour calibration and texture mapping modes can be used to help improve model texture and poorly focused images can be excluded to improve resulting texture quality.

Rigid Body Animation

The XMALab motion data was integrated with the photogrammetric models using the 3D computer graphics package Autodesk Maya (Autodesk Inc., San Rafael, CA, USA). Due to its wide range of 3D modelling and animation tools, custom-written scripts for XROMM animation and analysis,

combined with it being free for academic use, Maya has become an integral part of the XROMM workflow (Bonnan et al, 2016).

The 3D models created in Metashape are imported into Maya and aligned into reference poses to provide consistent starting positions and joint axes. Once the 3D models are transferred into Maya and oriented into reference poses, the XROMM Maya toolbox (available at https://bitbucket.org/xromm/xromm_mayatools/wiki/Home) is used to integrate the rigid body transformations in XMALab with the 3D models.

To provide file references for the rigid body transformations in XMALab, the centroid of the vertices of each marker in Maya are calculated using the vertAvg function (XROMM Maya Tool script, vAvg) and a locator placed. Once locators are placed along all the markers, they are then exported from Maya as CT coordinates, before being imported into XMALab and assigned to the appropriate markers. Once the rigid body transformations are calculated, they are then exported from XMALab, imported into Maya and applied with the 3D models (XROMM Maya Tool script 'imp').

The MayaCams from XMALab were imported into Maya so that the animation could be viewed against the original video images – enabling me to confirm whether the animation matched the motion in the video. Where there was a visible mismatch, the bone models were manually rotoscoped (Gatesy et al., 2010).

To calculate rotations/translations in Maya, joint co-ordinate systems (JCSs) are used. A JCS is a set of orthogonal axes that measures the translations and rotations between two rigid bodies – in this case, a JCS is used to measure the pose of a distal "child" segment relative to its proximal "parent" segment. The JCSs are set and aligned using the jAx tool (XROMM Maya Tool script, jAx). The Maya Graph Editor can be used to view JCS kinematics versus time graphs and observe how movements occur over time.

Conclusion

The total hardware cost for the experimental setup was less than £550 (not counting the laptop computer used for data analysis, or the photogrammetry camera), with two comparatively inexpensive GoPro cameras (~£270 each) used to collect video footage and a calibration object made of LEGO bricks (< £5). Photogrammetry was carried out using a comparatively inexpensive Sony NEX-6 digital camera (~£500) - however, it is important to note that photogrammetry is compatible with any brand of camera, including smartphone cameras or even the GoPro cameras used to record video. Of the software used, only one was commercial – Metashape – ($59 for educational use), though open-source alternatives are available (Falkingham 2012).

Equipment needed
GoPro Hero 7 Black cameras (x2)
WiFi remote
LED light on tripod
Mobile phone stopwatch
LEGO calibration object
Laptop computer (for data analysis)

Table 2.1 - All equipment used in study

A data capture session using the workflow roughly lasts about 2-5 minutes (using the optimum configuration, see next chapter), whilst data analysis can take up to 1 week, depending on the number of markers that need to be analysed, and the length of the recording.

3 Accuracy and precision of the GoPro camera setup
Assessing the impact of different camera settings on accuracy and precision in XMALab

Introduction

The primary aim of the experiments carried out in this chapter was to assess the precision and accuracy of the GoPro-based experimental setup that will be used for *in vivo* data collection in the next chapter. To do so, a wand made from LEGO bricks was tracked using the workflow outlined in the previous chapter. In assessing accuracy and precision, I will ascertain how, if at all, differing camera settings might affect the performance of marker tracking in XMALab, and overall quality of the workflow.

For the purposes of this experiment, accuracy is defined as the difference between the actual distance and the mean distance recorded in XMALab, whereas precision is defined as the variation of the recorded distance over time (in accordance with Brainerd, 2010). It is important to ascertain the accuracy and precision, as these determine the range of translations and rotations that can be reliably measured (Menegaz et al, 2015).

Materials and Methods

To determine the accuracy and precision of 3D marker tracking from video data, several trials were performed tracking six markers placed at a known distance on a LEGO wand (Figure 1). All six markers were tracked and accuracy and precision was measured based on the reconstructed distances between markers 1 and 3 (actual distance 80.00mm) and markers 2 and 6 (actual distance 35.00mm).
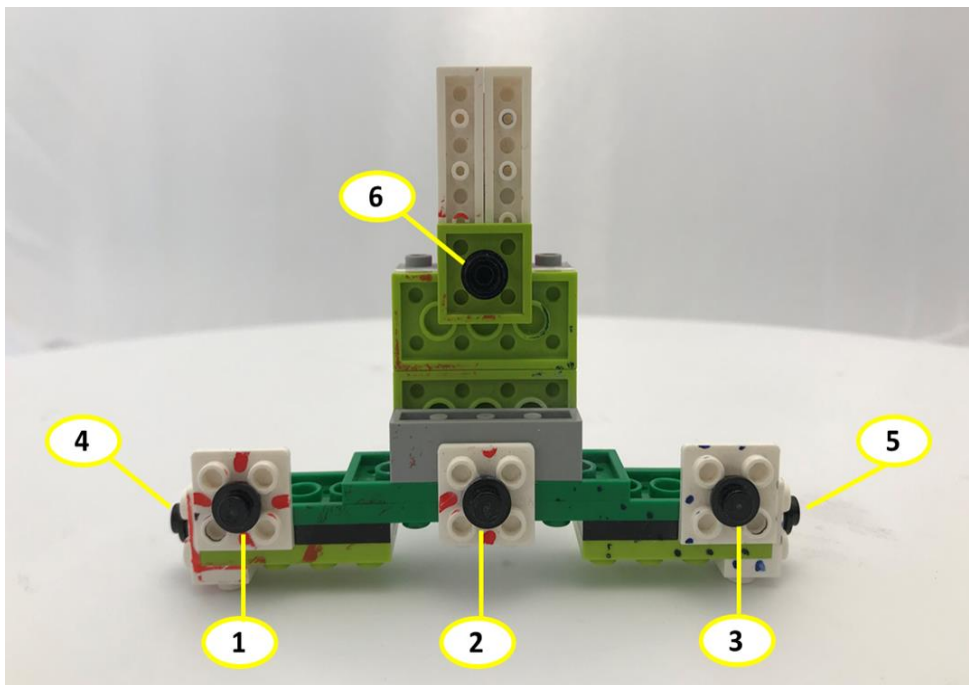
Figure 3.1 - LEGO marker wand - the six markers labelled are in black and tracked in XMALab

To capture footage, two GoPro cameras were placed at ~45 degrees to each other, facing the wand, and 3 seconds of footage captured while the wand was moved through the imaged volume. To maintain consistent light levels, an LED ring light on a tripod was used. The experiment was performed using three different field of views (FOVs) (Linear, Wide and Super-View), three different resolutions (1920x720p, 1920x1080p and 2704x1524p) and three framerates (30fps, 60fps and 120fps). Where settings allowed (since the highest framerates and linear field of view cannot be used at the highest resolutions) all combinations of the above were tested.

Camera calibration is required to calculate 3D co-ordinates of the markers from the 2D points tracked in each video. Starting with images of an object with known dimensions, the process generates a mathematical model of camera position and orientation in 3D space, as well as the camera's internal parameters (Knörlein et al. 2016).

For this experiment, the calibration object (see figure 2.1) was constructed out of LEGO blocks. The XYZ co-ordinates of each raised nub were entered into a CSV file based on known LEGO dimensions (see previous chapter). To speed up the process of identifying all the markers, four specific nubs were chosen as reference points, enabling me to semi-automatically identify the 2D locations of all the markers based on those points, with a separate .ref file created with this information (see previous chapter). Images of the LEGO calibration object were recorded for each trial, with trials being carried out where the calibration object was placed in only a single position, as opposed to the multiple positions in all other trials. For the latter, the calibration object was placed in six positions in total, with positions chosen based on the field of view of the cameras and the object placed in areas where they overlapped, encompassing the entirety of the field of view, enabling 3D co-ordinates of the markers 2D positions, as well as camera position, orientation and spacing to be calculated for the whole field of view.

TRIAL NO.	RESOLUTION (P)	FRAMERATE (FPS)	SINGLE OR MULTIPLE CALIBRATION POSITIONS	FIELD OF VIEW
1	1920x1080	60	Single	Linear
2	1920x1080	60	Multi	Linear
3	1920x1080	60	Multi	Linear
4	1920x1080	60	Multi	Wide
5	1920x1080	60	Multi	Super-View
6	1280x720	60	Multi	Linear
7	1920x1080	60	Multi	Linear
8	1524x2704p	60	Multi	Linear
9	1920x1080	30	Multi	Linear
10	1920x1080	60	Multi	Linear
11	1920x1080	120	Multi	Linear

Table 3.1 - All configurations tested – single vs. multi, field of view, resolution, framerate. P is pixels and fps is frames per second. Trials 1-2 tested single or multi positions of the calibration object, all other variables constant. Trials 3-5 explored the effects of field of view. Trials 6-8 investigated the effects of resolution, all other parameters constant, and finally trials 9-11 tested the effects of framerate.
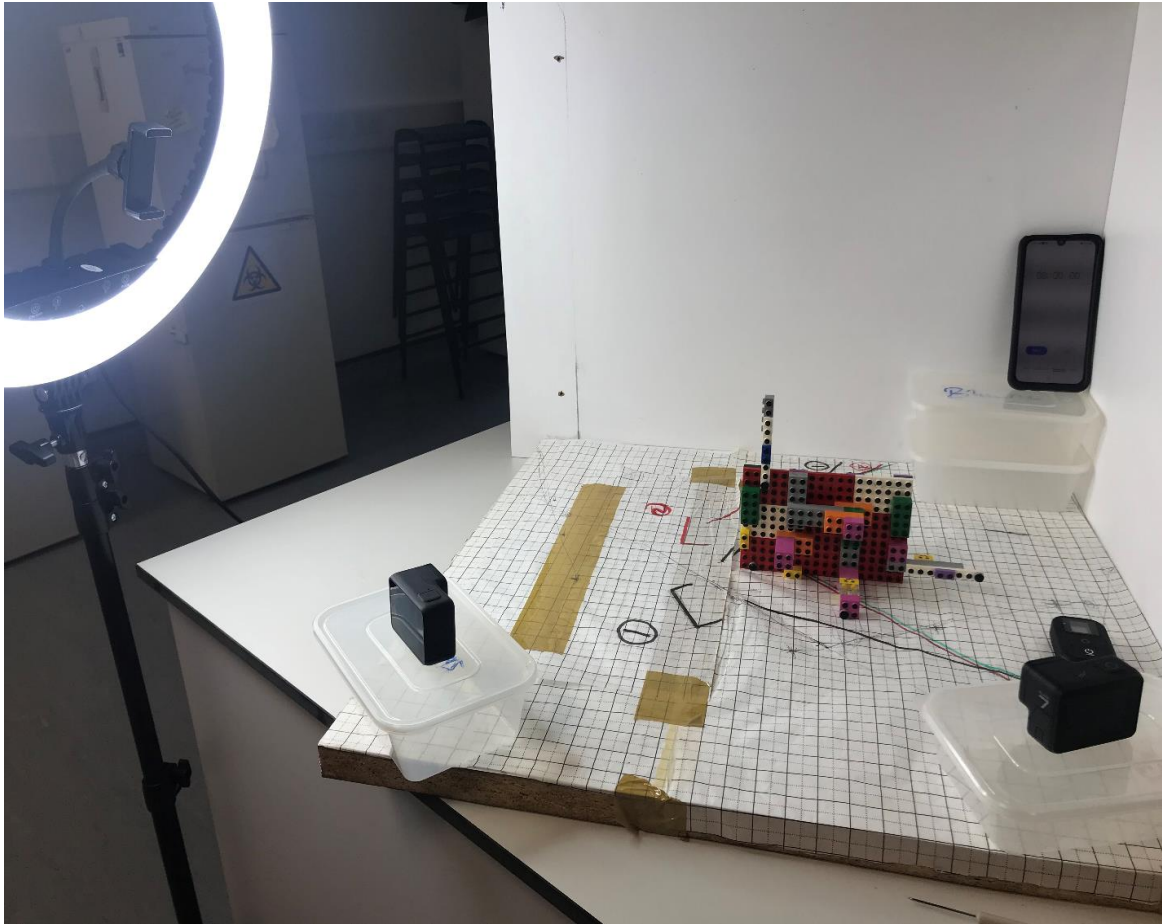
Fig. 3.2. Study setup for calibration object. GoPro cameras (left and right in foreground), along with the remote control (far-right in foreground). LED ring light (far left), used to maintain consistent light levels, mobile phone (used to record time) and, in centre, calibration object

Once the calibration videos had been recorded, the LEGO wand was waved in a figure-of-eight approximately 30cm across at a slow speed, trying to ensure that all tracker points were visible to both cameras throughout the footage, at a distance of 20cm in front of the GoPro cameras for a period of three seconds. To assess within-frame accuracy, the LEGO wand was moved in an arc 8cm wide in front of the cameras. Because volume viewed by both cameras is not a simple cube, it was difficult to move the wand in such a way as to provide complete coverage of both images.

The GoPros were triggered through the use of a Wi-Fi remote and a mobile phone stopwatch was recorded by both cameras in each trial to later ensure that the cameras were properly synchronised. This was because, when triggered using the Wi-Fi remote, one of the cameras would start recording between 2-4 frames later (or 0.033-0.066 seconds) than the other.
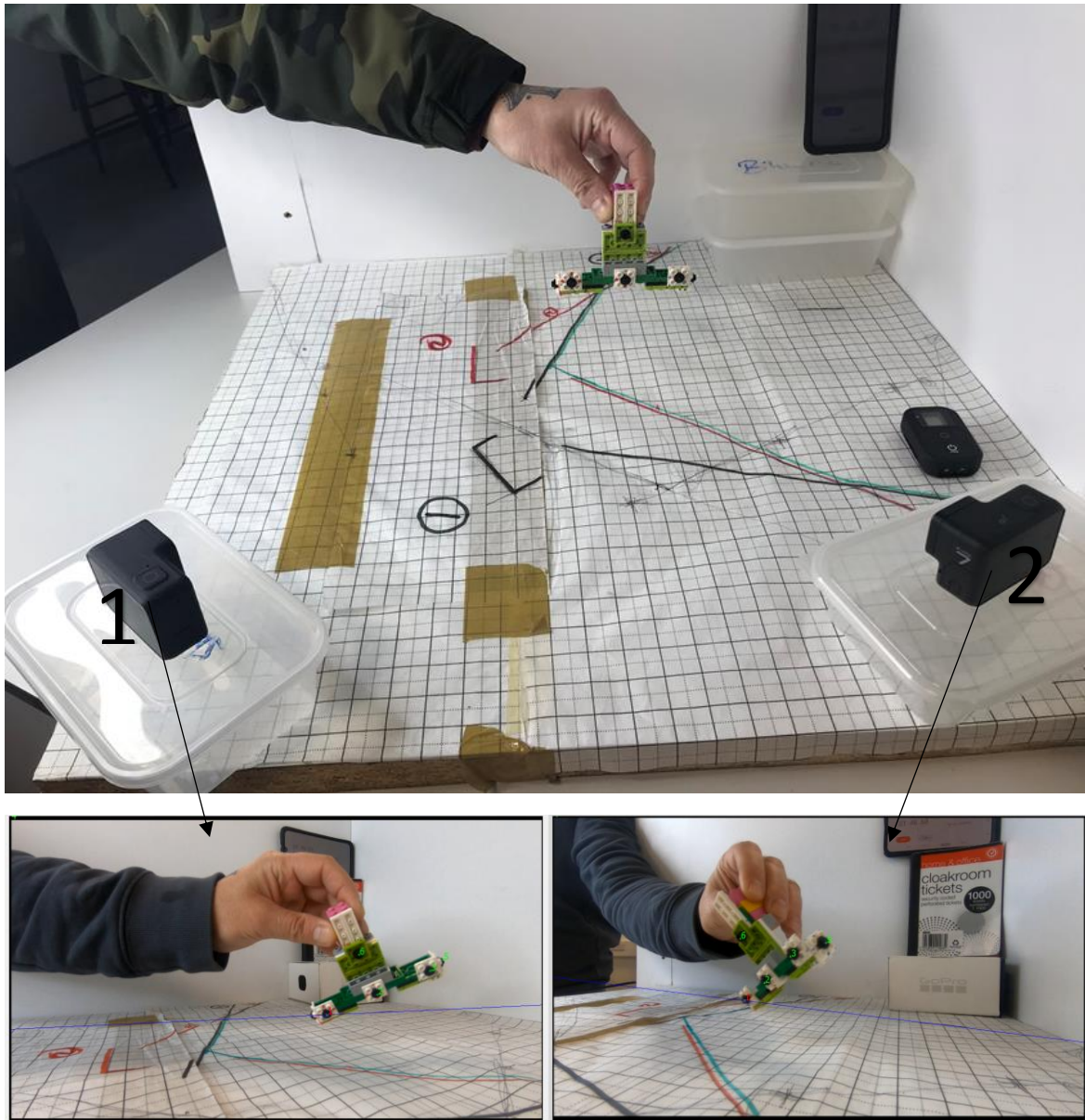
Fig. 3.3. Sample images of video frame (bottom two images) and study setup for marker tracking (top image). GoPro cameras (left and right in foreground), along with the remote control (far-right in foreground). In the background, mobile phone (used to keep time) and, in centre, LEGO wand

Videos were synchronised using the Video Editor in Blender, temporally aligning the videos so that the stopwatch was at the same time in both videos, before being exported as AVIs and imported into XMALab where the individual markers were tracked.

In accordance with previous studies (Knorlein et al, 2016; Brainerd et al, 2010; You et al, 2001), the mean inter-marker distance between the first and third markers (horizontal) and second and sixth (vertical) markers), with real values of those dimensions were 80.00 mm and 35.00 mm respectively (within the 0.002mm tolerance of LEGO) was used as a measure of accuracy, and the standard deviation of the inter-marker distance was used as a measure of precision. The mean reprojection error, which relates to the accuracy of camera calibration (how well can a point in one camera be identified in a second – and how well 3D co-ordinates can be reconstructed from 2D co-ordinates), of all six markers was also reported for each configuration.

Statistical analysis was carried out on the data using SPSS (Version 28.0.1.1).

Results
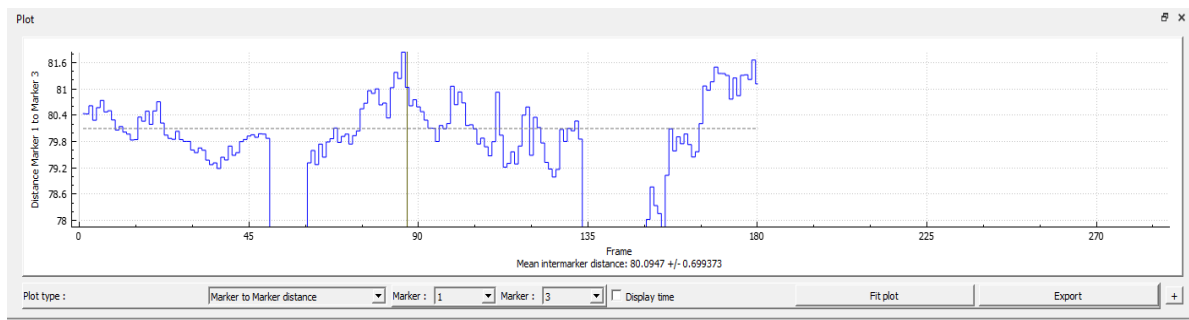
Fig. 3.4. Sample inter-marker distance graph from Trial 2 (multi-positioned calibration). Here, the mean intermarker distance is reported as 80.0947 mm, +/- 0.699373 mm. The true distance between these markers is 80.00 mm.

Of the individual settings, changing FOV settings had the greatest impact on accuracy and precision (with wide having the lowest accuracy and precision and linear having the highest) – followed by changing the resolution. Conversely, changes in framerate and differing calibration positions had a much smaller impact on accuracy and precision. Changing camera settings affected precision more than accuracy, with precision varying far more than accuracy between different camera settings.

Field of View

The accuracy and precision data for field of view was assessed for normality using a Shapiro-Wilk test and found to be mostly non-normally distributed – for the horizontal distance, $W(153) = 0.979$, $p = 0.017$ for linear, $W(145) = 0.686$, $p = <0.01$ for wide-angle and $W(126) = 0.986$, $p = 0.228$ for super-view respectively, and, for the vertical distance, $W(142) = 0.878$, $p = <0.01$ in the linear field of view, $W(131) = 0.948$, $p = <0.01$ for vertical in the wide-angle field of view and $W(113) = 0.922$, $p = <0.001$ for super-view respectively.

FIELD OF VIEW	HORIZONTAL (MARKER 1 TO 3)				VERTICAL (MARKER 2 TO 6)			
	No. of frames tracked	Accuracy (mm)		Precision (mm)	No. of frames	Accuracy (mm)		Precision (mm)
		True Distance (mm)	Recorded distance (mean, mm)			True Distance (mm)	Recorded distance (mean, mm)	
LINEAR	153	80	80.09	0.70	142	35	34.96	0.15
WIDE	145	80	83.76	0.98	131	35	35.91	0.43
SUPER-WIDE	126	80	82.13	0.95	116	35	35.68	0.37

Table 3.2 - The effect of changes in field of view on accuracy and precision in marker tracking in XMALab

	Reprojection error (p)					
	Marker 1	**Marker 2**	**Marker 3**	**Marker 4**	**Marker 5**	**Marker 6**
Linear	0.11 (±0.08)	0.11 (±0.07)	0.13 (±0.09)	0.17 (±0.11)	0.06 (±0.06)	0.11 (±0.08)
Wide-Angle	0.60 (±1.59)	0.30 (±0.68)	0.41 (±0.77)	1.62 (±2.54)	0.10 (±0.11)	0.20 (±0.18)
Super-View	0.45 (±0.66)	0.38 (±0.45)	0.83 (±1.48)	0.84 (±1.63)	0.89 (±1.58)	0.38 (±0.33)

Table 3.3 – Reprojection error figures according to changes in field of view.

31

A Kruskal-Wallis H test showed that increasing the field of view significantly affected the accuracy and precision of both the horizontal and vertical distances, $\chi^2(2) = 333.68$, p = <.001, with a mean rank of 83.15 for linear, 342.31 for wide-angle and 220.18 for super-view for horizontal and $\chi^2(2) = 274.099$, p = <.001, with a mean rank of 72.06 for linear, 282.87 for wide-angle and 242.50 for super-view for vertical.

On average, accuracy and precision substantially decreased as FOV was increased – linear was both most accurate, and most precise. For the wide setting, XMALab recovered the known horizontal distance of 80.00mm to an accuracy of -3.77mm (-4.71%), with a precision of 0.98mm, and the known vertical distance to an accuracy of -0.91 mm (-2.61%) with a precision of 0.43mm.

For the Super-Wide FOV, XMALab recovered the known horizontal distance of 80mm to an accuracy of -2.11mm (-2.63%), with a precision of 0.99mm, and the known vertical distance to an accuracy of -0.06mm (-1.95%) with a precision of 0.37mm (see Table 3.2).

Resolution

The accuracy and precision according to changes of resolution was assessed for normality. A Shapiro-Wilk test found that the data was non-normally distributed – for the horizontal distance, W(120) = 0.938, p =<0.01 for 720p, W(153) = 0.978, p =0.017 for 1080p and W(122) = 0.899, p =<0.01 for 2.7kp and, for the vertical distance, W(107) = 0.967, p =.010 for 720p, W(143) = 0.881, p =<0.01 for 1080p and W(131) = 0.963, p =0.01 for 2.7kp.

An increase in camera resolution generally led to an increase in accuracy and precision, with the 2.7kp configuration having the highest accuracy and precision on both the horizontal and vertical distance – however, only very slightly in the case of the latter.

RESOLUTION (P)	HORIZONTAL (MARKER 1 TO 3)				VERTICAL (MARKER 2 TO 6)			
	Frames (n)	Accuracy (mm)		Precision (mm)	Frames (n)	Accuracy (mm)		Precision (mm)
		Real Distance (mm)	Recorded distance (mean, mm)			Real Distance (mm)	Recorded distance (mean, mm)	
720	120	80	79.40	0.91	107	35	34.59	0.33
1080	153	80	80.09	0.70	143	35	34.96	0.16
2.7K	122	80	80.02	0.68	131	35	34.97	0.11

Table 3.4 - Accuracy and precision measurements according to changes in resolution

Resolution (pixels)	Reprojection error (p)					
	Marker 1	Marker 2	Marker 3	Marker 4	Marker 5	Marker 6
720	0.12 (±0.1)	0.11 (±0.09)	0.17 (±0.22)	0.23 (±0.34)	0.34 (±0.58)	0.11 (±0.11)
1080	0.11 (±0.08)	0.11 (±0.07)	0.13 (±0.09)	0.17 (±0.11)	0.06 (±0.06)	0.11 (±0.08)
2.7k	0.23 (±0.14)	0.38 (±0.49)	0.18 (±0.14)	0.34 (±0.16)	0.21 (±0.13)	0.44 (±0.58)

Table 3.5 – Reprojection error according to changes in resolution

A Kruskal-Wallis H test showed that increasing the resolution significantly affected the accuracy and precision of both the horizontal and vertical distances, $\chi^2(2) = 77.983$, p = <.001 for the horizontal and $\chi^2(2) = 155.073$, p = <.001 for the vertical, with a mean rank of 121.72 for 720p, 237.54 for

1080p and 233.44 for 2.7kp for the horizontal distance and a mean rank of 78.71 for 720p, 238.85 for 1080p and 230.49 for 2.7kp for the vertical distance.

Framerate

The accuracy and precision according to changes of framerate was assessed for normality. A Shapiro-Wilk test found that the data was non-normally distributed – for the horizontal distance, W(153) = 0.978, p =0.017 for the single position and W(108) = 0.964, p =<0.005 for the multiple positions and, for the vertical distance, W(118) = 0.971, p =0.012 for the single position and W(143) = .881, p =<0.01 for the multiple positions.

A Kruskal-Wallis H test showed that increasing the framerate significantly affected the accuracy and precision of both the horizontal and vertical distances, χ2(2) = 64.584, p = <.001, with a mean rank of 143.65 for 30fps, 296.55 for 60fps and 208.06 for 120fps for horizontal and χ2(2) = 108.919, p = <.001, with a mean rank of 122.05 for 30fps, 324.09 for 60fps and 203.71 for 120fps.

Changing the framerate had a slight, but significant effect on accuracy and precision, aside from a slight decrease in precision for the horizontal distance when the framerate was increased - however, a higher framerate did lead to a substantially decreased reprojection error.

When the framerate was increased to 120fps, XMALab recovered the known horizontal distance of 80mm to an accuracy of -0.33mm (0.4%), with a precision of 0.87mm, and the known vertical distance to an accuracy of 0.24mm (0.67%) with a precision of 0.15mm.

FRAMERATE (FPS)	HORIZONTAL (MARKER 1 TO 3)				VERTICAL (MARKER 2 TO 6)			
	Accuracy (mm)			Precision (mm)		Accuracy (mm)		Precision (mm)
	Frames	Distance (mm)	Accuracy (mean, mm)		Frames	Distance (mm)	Accuracy (mean, mm)	
30	46	80	79.34	0.87	46	35	34.52	0.37
60	153	80	80.09	0.70	153	35	34.96	0.16
120	246	80	79.67	0.67	262	35	34.76	0.15

Table 3.6 - The effect of changes in framerate on accuracy and precision measurements

	Reprojection error (p)					
Framerate (fps)	**Marker 1**	**Marker 2**	**Marker 3**	**Marker 4**	**Marker 5**	**Marker 6**
30	0.14 (±0.12)	0.12 (±0.09)	0.15 (±0.14)	0.11 (±0.1)	0.51 (±0.57)	0.13 (±0.11)
60	0.11 (±0.08)	0.11 (±0.07)	0.13 (±0.09)	0.17 (±0.11)	0.06 (±0.06)	0.11 (±0.08)
120	0.10 (±0.07)	0.88 (±0.06)	0.11 (±0.08)	0.11 (±0.08)	0.12 (±0.08)	0.1 (±0.07)

Table 3.7 – The effect of changes in framerate on reprojection error

When the framerate was reduced to 30fps, XMALab recovered the known horizontal distance of 80mm to an accuracy of 0.66mm (0.82%), with a precision of 0.87mm, and the known vertical distance of 35mm to an accuracy of 0.48mm (1.38%) with a precision of 0.37mm.

Single versus multiple calibration object positions

The accuracy and precision data for single vs. multi calibration positions was assessed for normality using a Shapiro-Wilk test and found to be non-normally distributed, W(142) = 0.878, p =<0.01 in the linear field of view and W(116) = 0.956, p =<0.01 for super-view for the horizontal distance, W(142) = 0.878, p =<0.01 for linear and W(116) =0 .956, p =<0.01 for super-view.

Positioning the calibration object at multiple positions led to a slight, but significant increase in accuracy and precision (U = 4161, p =<0.01 for the horizontal distance, U = 2113, p=<0.01 for vertical), as well as a decrease in reprojection error, compared to only a single calibration position. From the measurements for the multiple positioned calibration object, XMALab recovered the known horizontal distance of 80mm to an accuracy of -0.09mm (-0.118%), with a precision of 0.7mm, and the known vertical distance to an accuracy of 0.0389mm (0.111%) with a precision of 0.15mm (Table 3.4).

SINGLE VS. MULTIPLE CALIBRATION POSITIONS	HORIZONTAL (MARKER 1 TO 3)				VERTICAL (MARKER 2 TO 6)			
	Accuracy (mm)		Precision (mm)		Accuracy (mm)			Precision (mm)
	Frame	Distance (mm)	Accuracy (mean, mm)		Frame	Distance (mm)	Accuracy (mean, mm)	
SINGLE	153	80	79.43	0.74	118	35	34.44	0.43
MULTIPLE	108	80	80.09	0.70	143	35	34.96	0.15

Table 3.8 - The effect of single versus multiple calibration positions on accuracy and precision

	Reprojection error (p)					
	Marker 1	Marker 2	Marker 3	Marker 4	Marker 5	Marker 6
Single	0.13 (±0.1)	0.16 (±0.13)	0.15 (±0.12)	0.18 (±0.16)	0.13 (±0.1)	0.13 (±0.12)
Multi	0.11 (±0.08)	0.11 (±0.07)	0.13 (±0.09)	0.17 (±0.11)	0.06 (±0.06)	0.11 (±0.08)

Table 3.9 – Reprojection error figures for the single versus multiple calibration positions.

When the calibration object was placed in a single position, XMALab recovered the known horizontal distance of 80mm to an accuracy of 0.57mm (0.71%), with a precision of 0.74mm, and the known vertical distance to an accuracy of 0.56mm (1.6%) with a precision of 0.43mm.
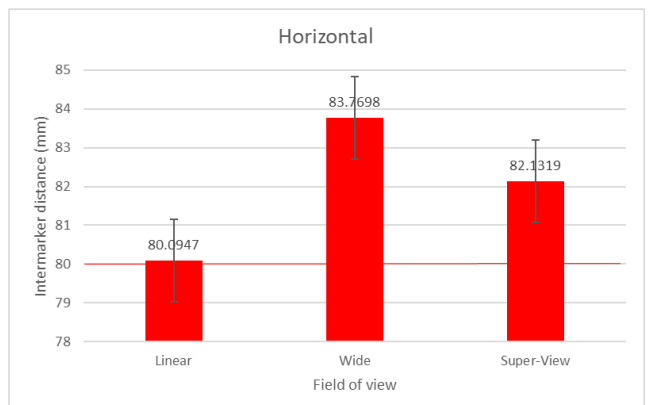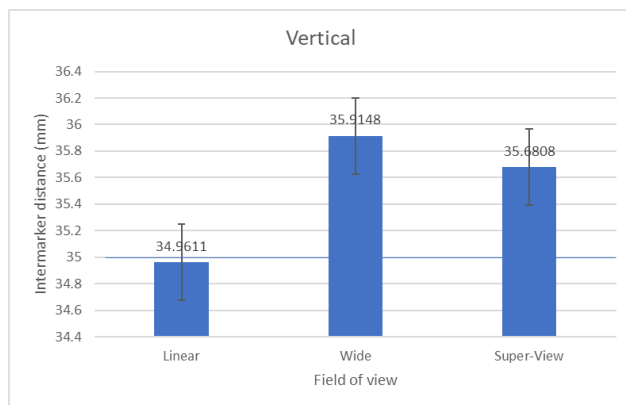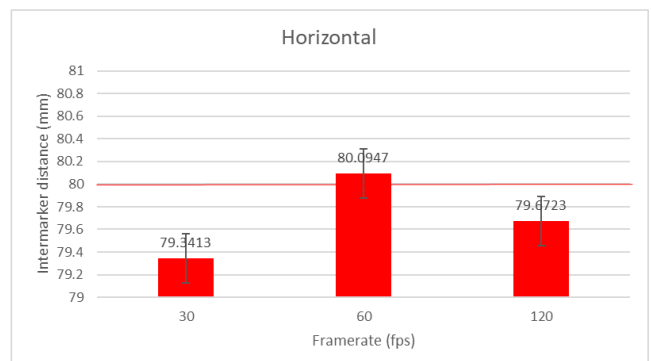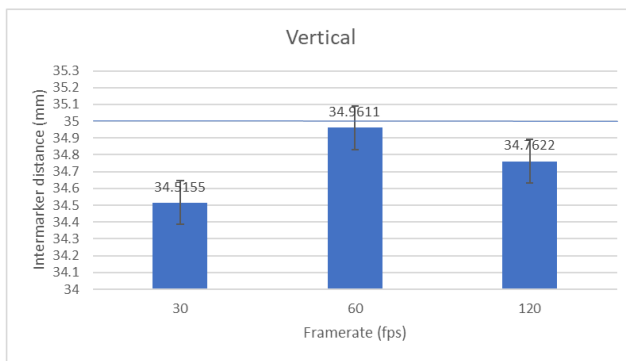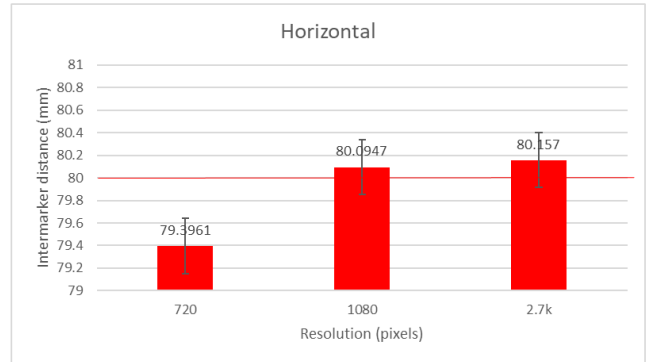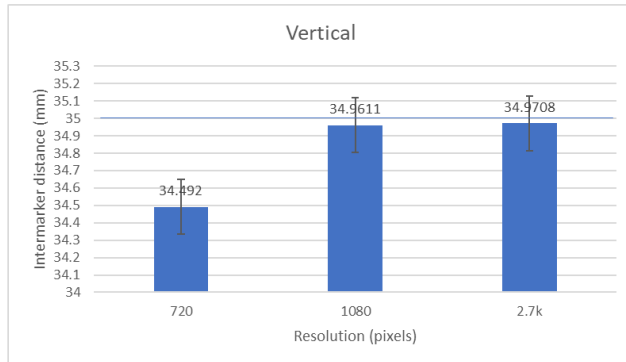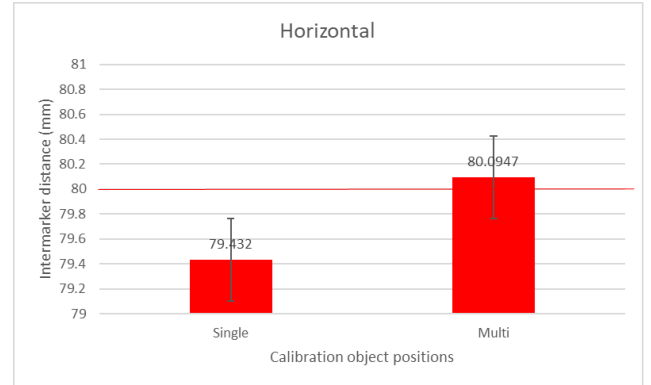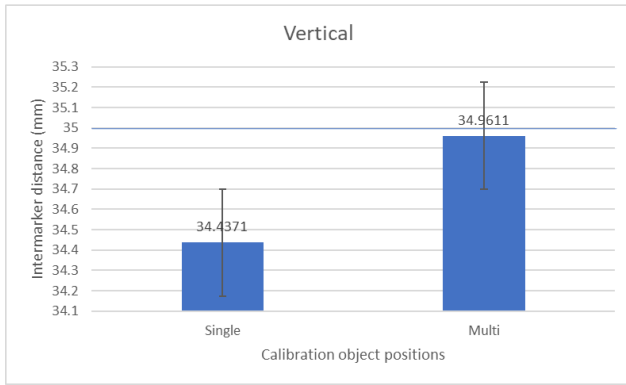
Fig. 3.5. Accuracy figures for marker tracking in XMALab – a) single vs. multi, b) resolution, c) framerate, d) field of view.
Real intermarker distance is represented by a coloured line and measured intermarker distance is represented by a coloured bar– horizontal (blue), vertical (red).
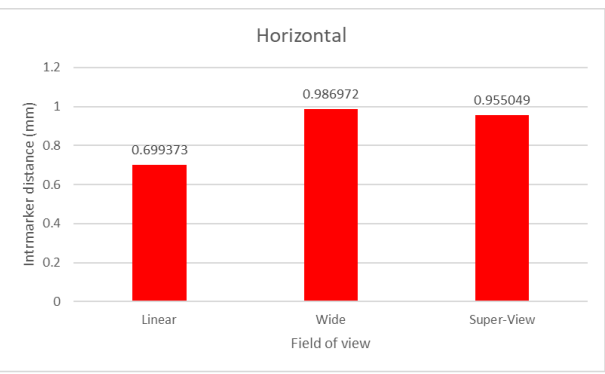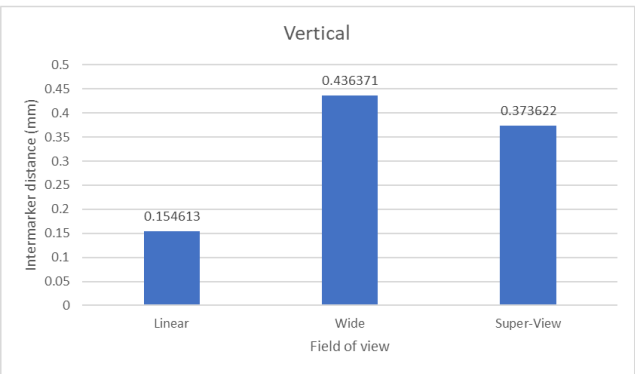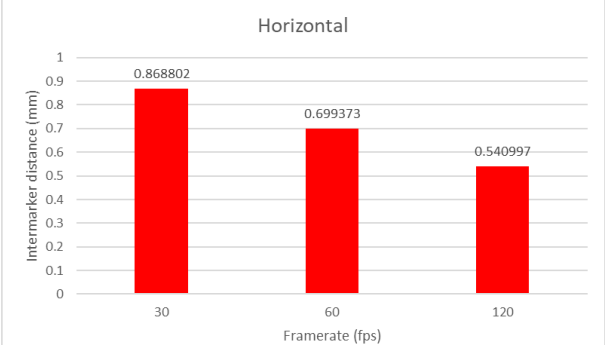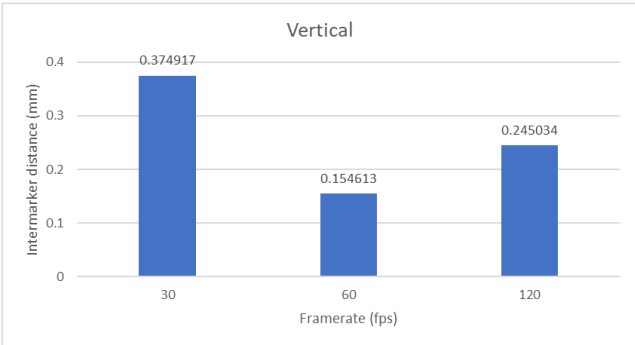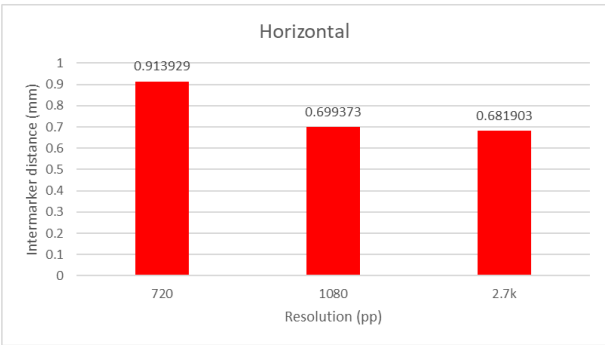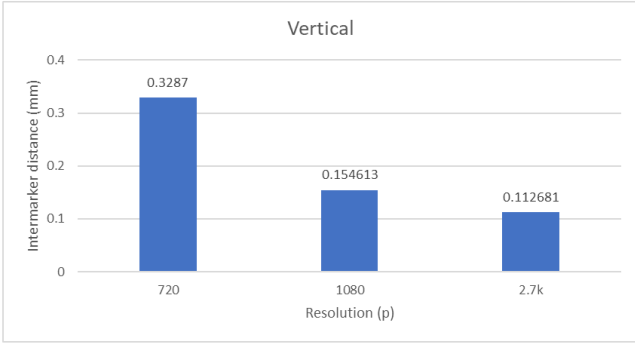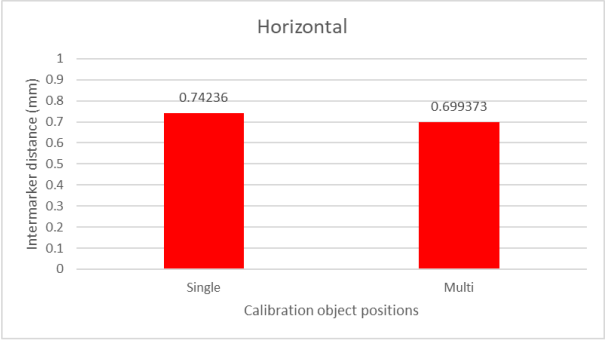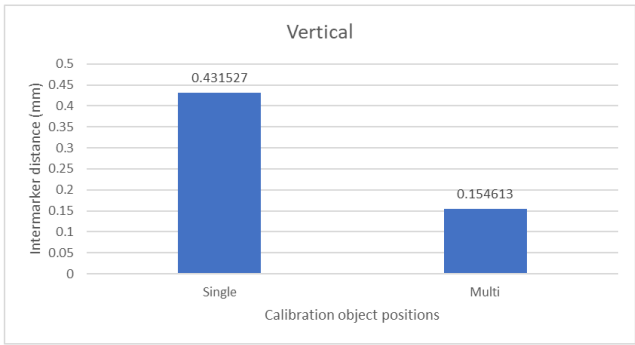
Figure 3.6. Precision figures for marker tracking in XMALab – a) single vs. multi, b) resolution, c) framerate, d) field of view. The lower the value, the greater (better) the precision.

Within-frame accuracy

As field of view changed, within-frame accuracy (the variation in accuracy in different areas of a single frame) on the edges of the frame substantially decreased, with accuracy becoming less consistent and showing a greater degree of variability. For all three settings, accuracy was highest in the centre of the frame and lowest at the edges.
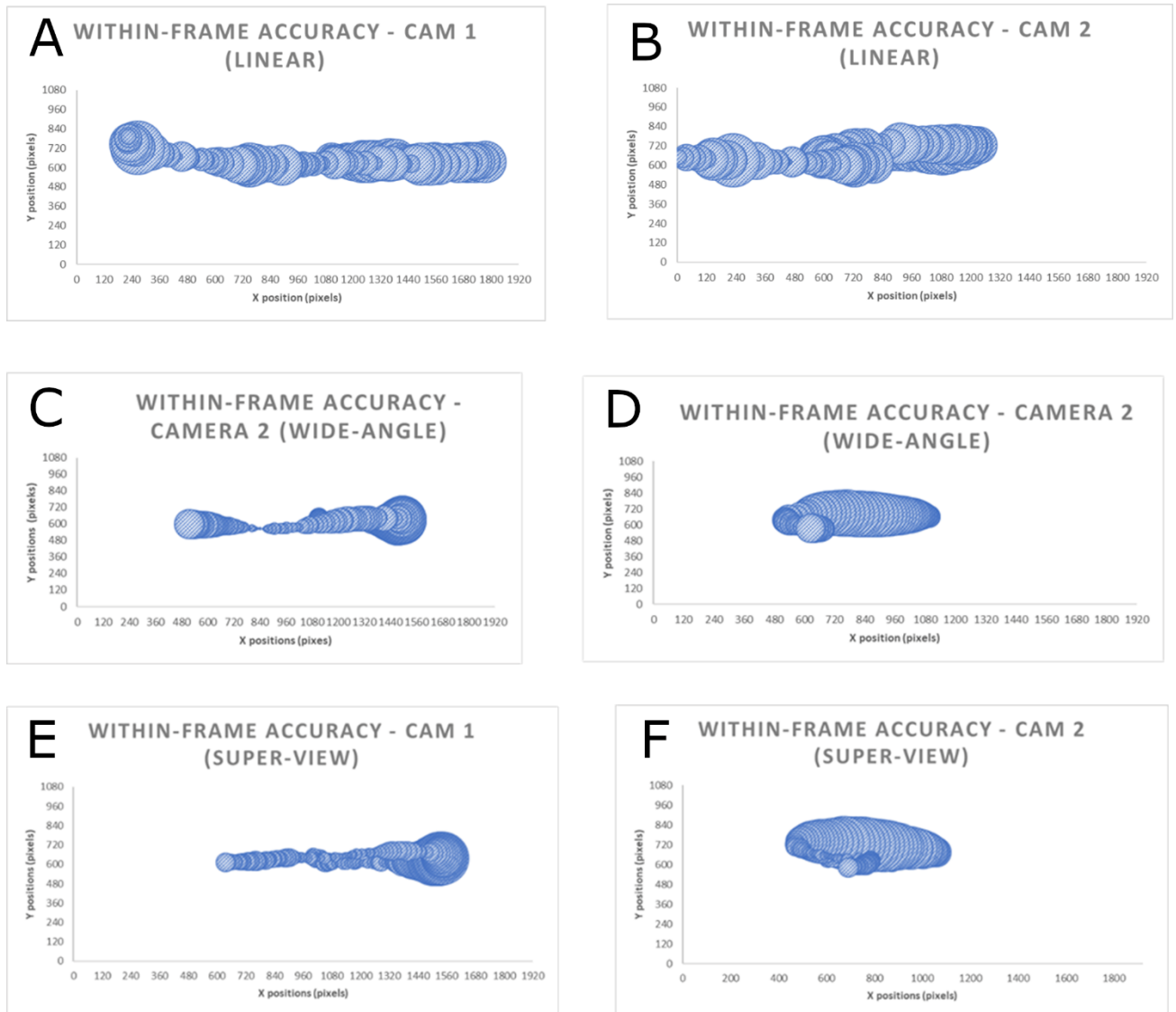
Figure 3.7. Accuracy within frame for camera 1 (A-C) and 2 (D-F) at linear (A,D), Wide (B,E) and Super-wide (C,F) field of views. Resolution and framerate were set to 1920x1080 and 60fps respectively. Smaller circles indicate higher accuracy (intermarker distance closest to real values), based on calculated distance between markers 1 and 3. Note that smallest circles generally appear in the centre of the imaging volume. As the object moves away from the centre of the frame, relative accuracy decreases (represented by the wider bubbles – all are scaled the same).

Discussion

From the results, it is clear that changes in camera settings had an impact on accuracy and precision to varying degrees. In the following discussion, the impact of the individual changes will be clarified.

Single vs. multiple calibration object positions

Placing the calibration object in multiple positions led to a slight increase in accuracy and precision. This is because placing the calibration object in multiple positions enabled 3D co-ordinates of the 2D positions of the markers, as well as the camera position, orientation and spacing, to be calculated for the entirety of the field of view, rather than interpolated from a smaller portion of the imaged volume.

Whilst the increase in accuracy and precision is marginal, it is important to note that this is rather easy to implement and does not greatly increase the time taken to collect or process the data. Therefore, even though the effect on accuracy and precision is relatively minor, placing the calibration object in multiple positions is recommended.

Field of View

Accuracy and precision, both overall and within-frame, substantially decreased when FOV was increased. This is most likely because a change in FOV leads to a greater degree of distortion in the image (as seen in figure 3.9), negatively affecting accuracy and precision due to a greater degree of deformation, increasing the distance in XMALab compared to the actual distance and making individual markers less identifiable. Undistortion is an important part of the XROMM workflow to remove S-shaped or pincushion distortion created by non-linear X-ray beams, which can be bent by magnetic and electric fields. The superwide view of the GoPro cameras is partially undistorted in-camera by the GoPros, but further undistortion could be carried out manually in video editing software. However, the superwide view does mean that objects within frame are much smaller, and therefore harder to track accurately and precisely.
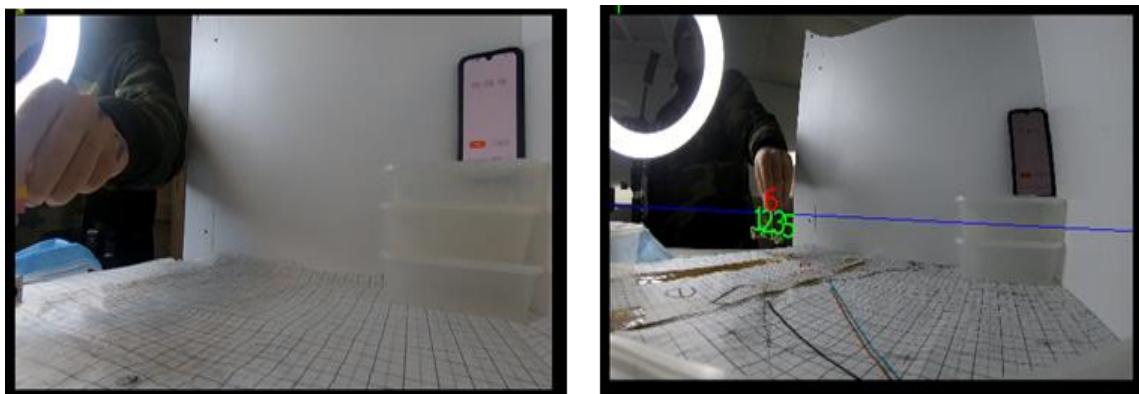
Figure 3.8. Images in the linear field of view (left) and wide-angle (right). Note the distortion in the right image.

Accuracy and precision figures for superwide were slightly higher than Wide Angle – a reason for this could be that, in that FOV, the distortion is greatest on the edges of the frame, whilst the wand was mostly at the centre.

As field of view was changed, within-frame accuracy increased in variability, becoming less consistent - the setting with the most consistent and highest accuracy was 'linear'. This is most likely

because of the decrease in distortion in the image, which varies across the frame (being highest at the edges and lowest in the middle).

Resolution

Increasing the resolution led to an increase in accuracy and precision, as can be seen from the higher average accuracy and precision values seen in the 2.7kp configuration, compared to the other two resolutions.

This is because, at higher resolutions, the markers were represented with an increased number of pixels. This led to an improved picture quality and an increase in detail, meaning that individual markers were more precisely identifiable, thereby increasing the efficiency of marker tracking in XMALab. However, this does create larger file sizes, which in turn can slightly slow down the process of marker tracking (because XMALab takes slightly longer to load each frame).

Framerate

Whilst changes in framerate had little effect on accuracy and precision overall (aside from a slight decrease in accuracy and precision on the vertical distance), increasing the framerate did lead to a decreased reprojection error for the horizontal distance. A possible reason as to why this could be, is that whilst picture quality is unaffected, an increase in framerate leads to an overall smoother shot, and more precise manual synchronization is possible.

Of course, it is possible that an increase in framerate would have a more significant effect on accuracy and precision if the LEGO wand were to be moved at a faster or slower speed – further experimentation would be needed to clarify this.

A major pitfall of an increase in frame rate is it will lead to increased processing time in XMALab – as seen in the 120fps configuration (which also had a lower accuracy and precision), because the number of frames to be tracked doubles when fps doubles (compared to for the 60fps trial). Whilst a decrease in framerate (30fps) did reduce processing time in XMALab, it was lower in accuracy and precision than the other two framerates. Based on these considerations, the optimal framerate is 60fps, the most accurate and precise of the framerates tested.

<u>Conclusion</u>

Of all the settings, widening field of view had the greatest negative impact on accuracy and precision, due to the greater degree of distortion in the image, and reduced number of pixels covering the area of interest. Additional manual undistortion may alleviate this, but this adds considerable post-processing time, and the issue of object size within frame remains. Increasing resolution had a positive impact on accuracy and precision, due to the increase in detail of the image. Changes in framerate and object position had less of an effect – however, framerate had a minor positive effect on reprojection error.

When considering optimum settings, it is important to note that a balance has to be struck between accuracy, precision and reprojection error throughout the trials. A further issue that should be taken into account is length of time analysing data in XMALab, which framerate in particular affected. Taking all these considerations into account, I concluded that the ideal setting is 2.7k resolution at60fps in the linear field of view, which offers the best compromise between accuracy, precision, reprojection error and time-efficiency in analysis (as shown in Table 3.10).

FRAMERATE (FPS)	RESOLUTION (P)	SINGLE OR MULTI	FIELD OF VIEW
60	2.7K	Multi	Linear

Table 3.10 - Optimum camera settings for accurate and precise marker tracking.

4 Evaluating the effectiveness of the workflow on biological data

Analysing the effect of soft tissue on the range of motion of an ostrich (*Struthio camelus* foot)

Introduction

The study of joint mobility in fossil archosaurs, such as non-avian dinosaurs (hereafter "dinosaurs"), is important in establishing aspects of their *in vivo* appearance and behaviours, including locomotion, posture, behaviour, and paleoecology, as well as comparative inferences of evolutionary trends (Senter, 2006).

Traditionally, range of motion (ROM) estimates have solely used osteological manipulation as a basis (using bone-on-bone stops and disarticulation as criteria, for more detail on this, see chapter 1). However, the presence of soft tissues in the vertebrate appendicular joint significantly affects mobility both directly and indirectly (Manafzadeh and Padian, 2018). Since most of these soft tissues are lost in fossilisation, this poses a major problem for palaeontological studies into joint ROM, as it is a source of debate as to whether soft tissues restrict or enhance ROM at any given joint.

Historically the effect of missing soft tissues was paid little attention, which has led to multiple misleading interpretations of archosaur joint mobility (Manafzadeh and Padian, 2018). In recent years, there has been a shift in studies of functional morphology towards reconstructing soft tissues and attempting to quantify how soft tissue influences ROM, utilising comparisons with the extant phylogenetic bracket (Witmer, 1995) of dinosaurs (crocodylians and birds) and osteological correlates to soft tissue in fossil taxa.

The primary aim of this experiment is to evaluate the effectiveness of the workflow detailed in previous chapters on a more realistic case study: *in vivo* ROM in an ostrich (*Struthio camelus*) foot using a soft tissue removal treatment. Flightless ratites are preferred as *in vivo* comparisons for the pedal morphology of bipedal archosaurs (especially bipedal dinosaurs) due to closer pedal morphological similarities than crocodiles (White et al, 2016). The secondary aim is to evaluate the effect of the removal of soft tissue on ROM, and its possible inferences for fossil archosaurs.

Materials and Methods

An adult ostrich (*Struthio camelus*) foot was obtained from an ostrich farm. A mixture of thumb tacks and metal nails with approximate lengths of 30mm and thicknesses of 3mm, were used as markers. The strength of the bone meant that nails had to be implanted with the aid of a small hammer. This procedure was quite difficult, since the nails had to be implanted in such a way that they were firmly in the bone, still visible externally, but also resistant to falling out (which, unfortunately happened multiple times during the experiment, see below). At the same time, this process had to avoid causing too much damage to the bones. Similar work has been done in human feet, using surgically implanted bone pins to track bone motion when walking or running (Maiwad et al, 2017).

In addition, the phalanges were difficult to access, due to the thickness of the skin and the presence of articular cartilage at the end of the bones, meaning that it was hard to ascertain whether a nail was actually in the bone, even if it felt secure. Three markers were used for each bone (except for digit 3's claw and the tarsometatarsus, which both had four, the former because of its shape and the latter because of its larger size).

Pushpins were used on the tarsometatarsus and the claw because, in the case of the latter, the pushpin was applied in an area where the keratinous sheath was softer, whereas the

tarsometatarsus had thinner layers of soft tissue than the phalanges. Prior to trials commencing, the complete foot was laid on the table surface (Figure 4.10) and documented using photogrammetry.

Footage was taken using two GoPro Hero 7 Black cameras using the 2.7kp/60fps/Linear setting (based on findings detailed in Chapter 3) placed on Hama tripod stands at roughly 45 degrees to each other. In order to calibrate the cameras, an object made of LEGO blocks was used. (For more detailed information on the experimental setup, see Chapter 2). At the beginning of each recording, a pen was tapped in view of both cameras to aid with later synchronicity (so that videos could be aligned to the instant of the pen tap)
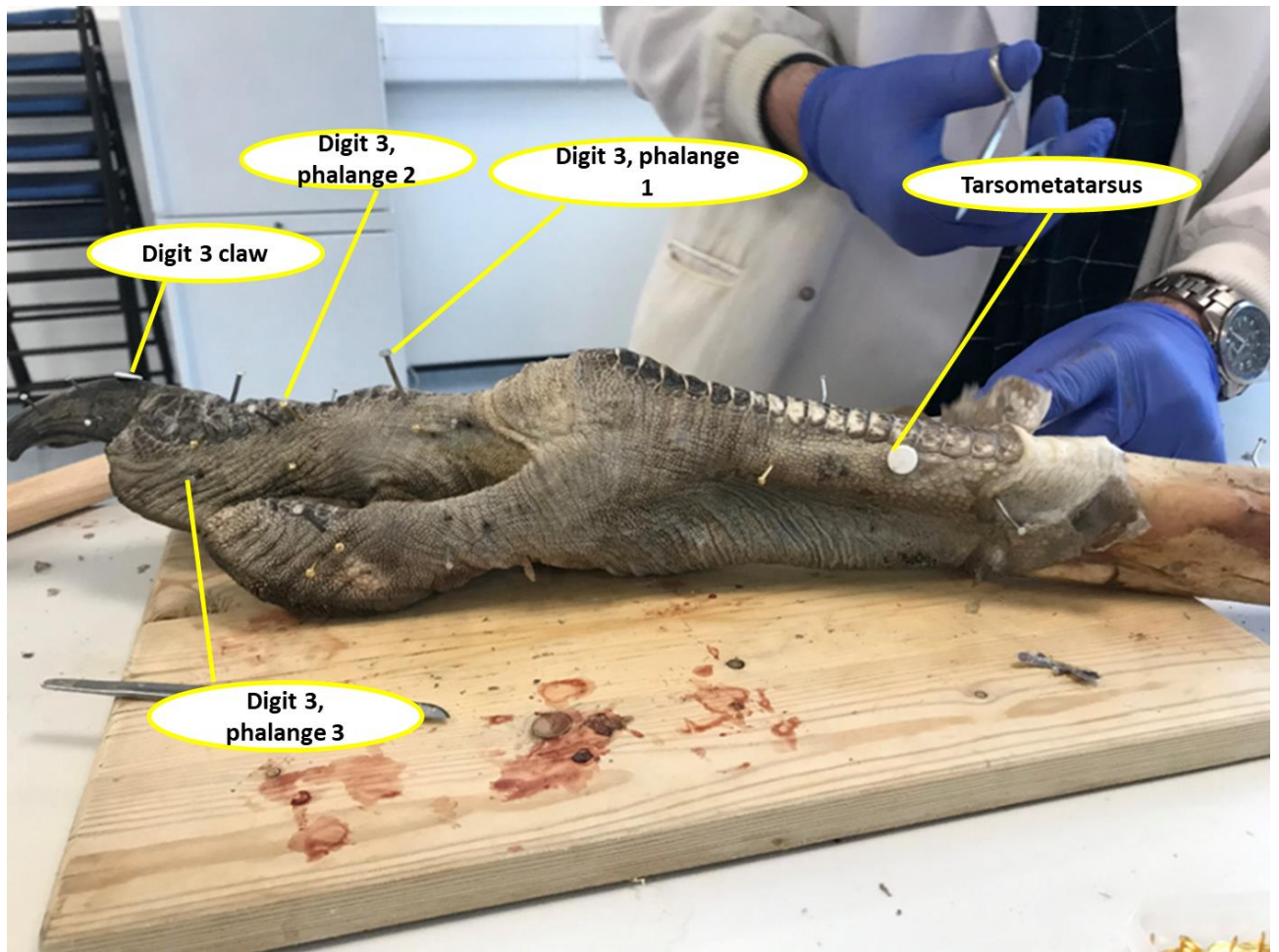
Figure 4.1 – The S. camelus *foot specimen that was used in the trials, prior to dissection.*
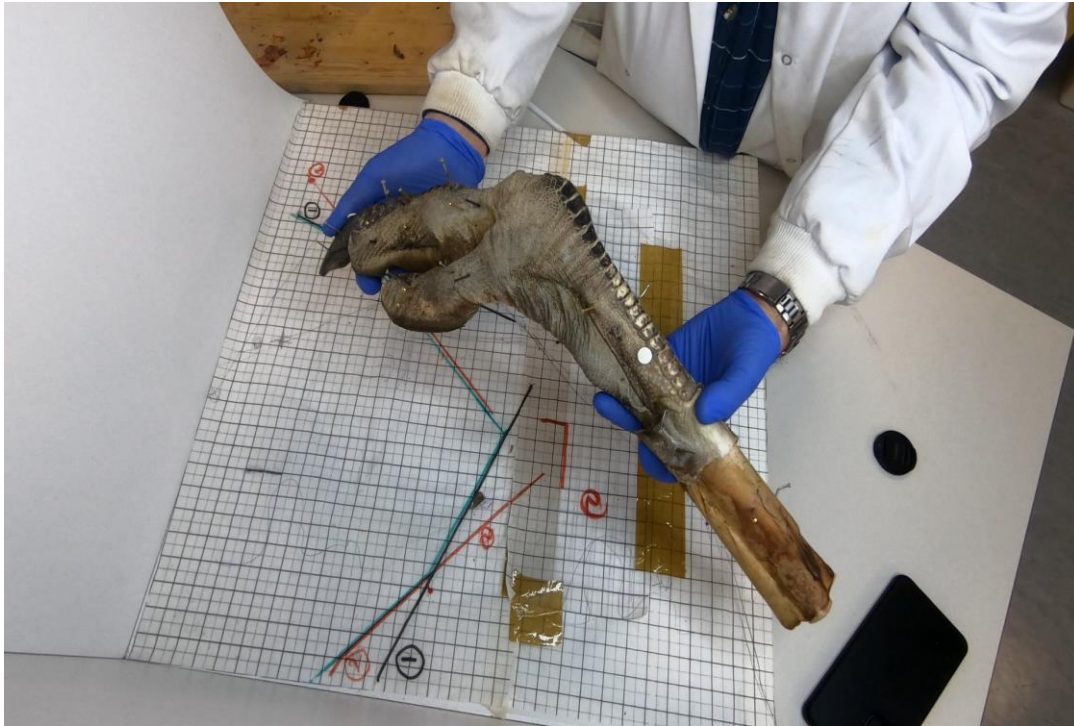
Figure 4.2 – The S. camelus foot specimen (skin-on) being held in flexed posture, viewed from Camera 1
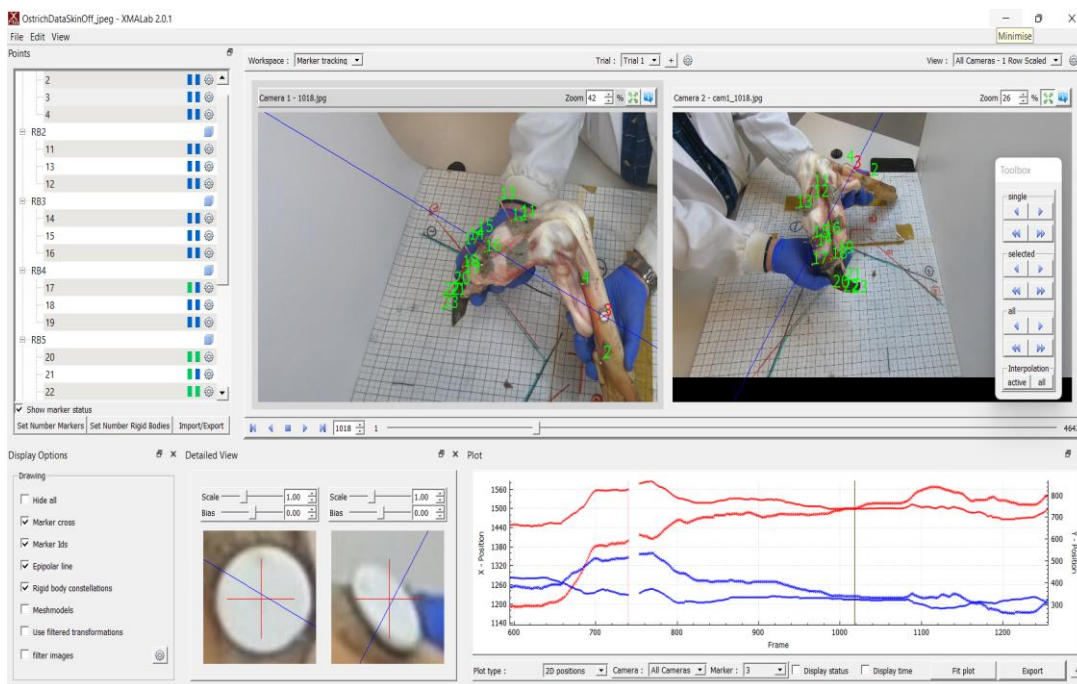
Figure 4.3 – Sample image of tracking of the skin-off trial in the Marker Tracking workspace in XMALab

The GoPro cameras were triggered remotely through vocal commands and the foot was held in the extension and flexion poses at three levels of sequential dissection – 1) all soft tissues (including integument) attached (skin-on); 2) integument removed (skin-off); 3) underlying musculature removed, leaving only tendons and ligaments on the bones (tendons). One trial was recorded for each level of dissection – three trials in total. The footage was then synchronised using the Video Editor capability in Blender before being clipped and exported into XMALab, where the individual markers were tracked.

After the footage had been taken, the specimen was then skeletonised using a slow cooker to remove all remaining tendons and articular cartilage. Once the specimen had been skeletonised, the bones were digitised using photogrammetry (Falkingham, 2012). Photographs were collected using a Sony NEX-6 digital camera with 18-50mm lens and the image set was loaded into the imaging software Metashape (agisoft.com) to create 3-D digital models of the bones.

To calculate rigid body transformations, XMALab requires digital bone models containing specific locations of each digitized marker. These were obtained by transferring the photogrammetric models of the bones into Autodesk Maya 2023 and arranging them in a reference pose. The pre-dissection photogrammetric model, and alignment of defleshed bone models to it, was used as an approximate osteological neutral reference pose (Kambic, Roberts and Gatesy, 2014). However, there were issues with the reference pose used – for instance, in the reference pose, the claw was slightly raised. This was because the phalanges were not aligned based on geometric calculations, but on where they naturally rested, meaning that 'zero' degrees rotation did not represent a mathematical alignment.

The centroids of each marker were calculated and a locator marking the xyz co-ordinates of the centroid was placed. Since some of the markers had been lost during skeletonization and during manipulations, a digital model of the intact foot, captured prior to dissection, was used to reconstruct 3D coordinates of lost markers. The model of the foot and the original bone models were scaled by a factor of 10 in Maya and the 3D models of the bones were matched to it based on the external markers consistent between pre- and post-dissection models.
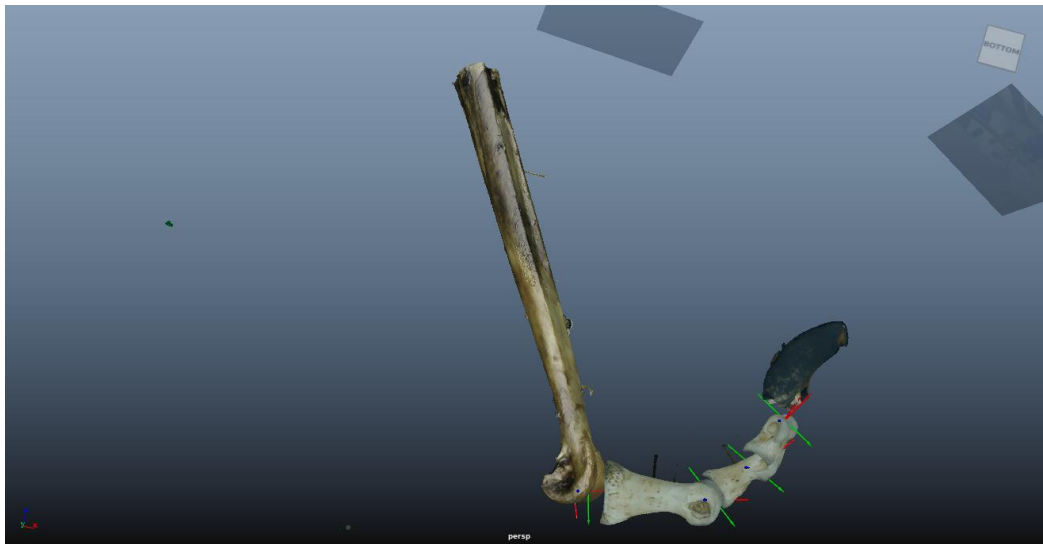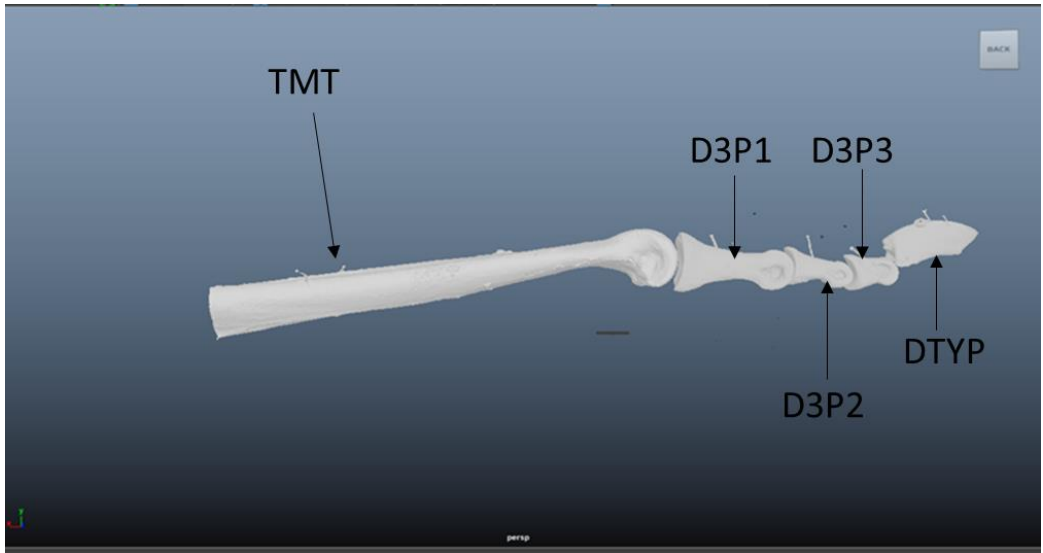
Figure 4.4 - Digital model of ostrich foot aligned in reference pose, with bones labelled (top), at maximum extension (middle) and maximum flexion (bottom). The camera planes in the background are positioned at roughly 45 degrees to each other. Note the presence of the jAx co-ordinate systems in this picture – x axis (red), y axis (green) and z axis (blue).

Once computed, the rigid body transformations were then imported into Maya 2023 using the "imp" script on the XROMM_MayaToolsPackage (available at https://bitbucket.org/xromm/xromm_mayatools/src/master/) to animate the bone models. To ensure Rigid Body Transformations (RBTs) matched footage, the GoPro camera positions and image planes were also imported into Maya (see figure 4.5).

When the bones were not aligned to the cameras' motions, because rigid body transformations were inaccurate or contained errors, scientific rotoscoping (Gatesy et al, 2010) was used to correct the alignment of the bones. In scientific rotoscoping, the motions of 3D bone models are manually rotated so that they match their positions on video data. Using the "PSDR" and "Ptrns" XROMM Maya scripts, the bone models were rotated and aligned to match (or overlay) their positions on the camera planes (using the markers that had been retained on the pre-and-post dissection models as reference), with changes in position being marked with key frames.
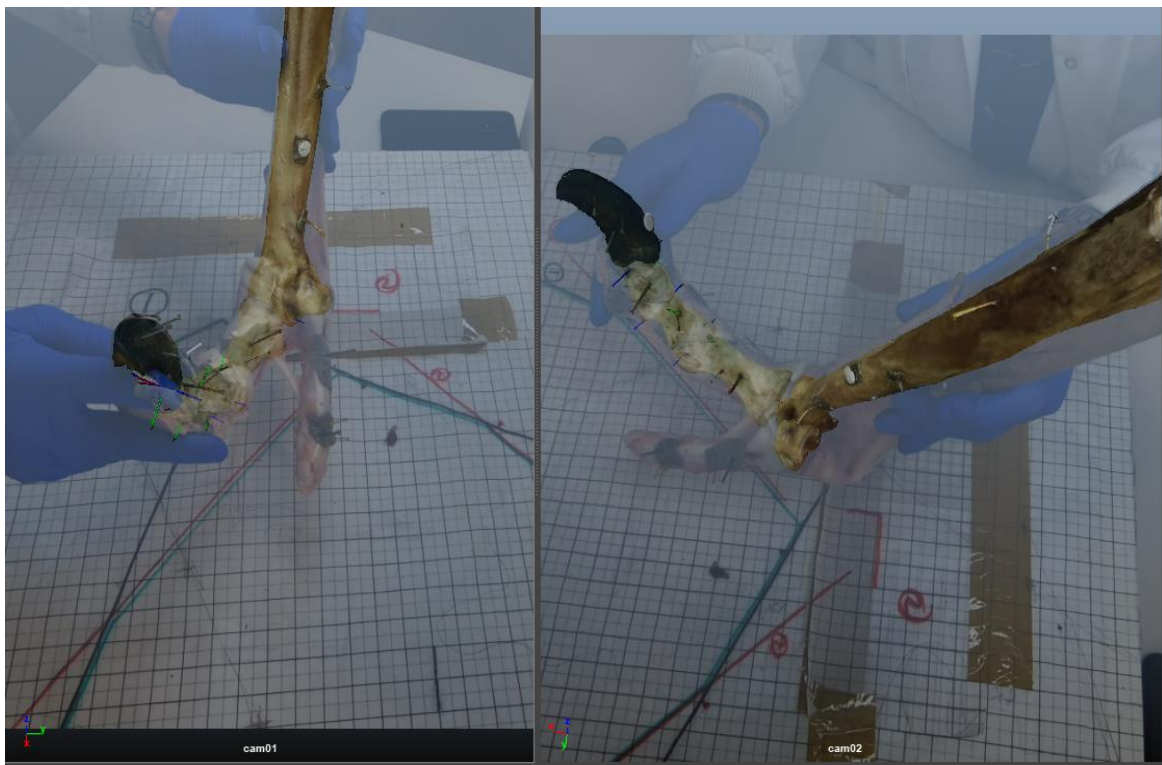
Figure 4.5 - X-ray cameras in Maya, used to ascertain whether bones are properly aligned. Note the 50% transparency X-ray cam view overlooking the bones.

In order to calculate bone rotation, joint co-ordinate systems were set at the reference pose and aligned with the bones using the "jAx" script, with locators being used to align two orthogonal axes where the proximal and distal segments articulated with each other (similar to the fitting of geometric primitives). The Z-axis represented flexion/extension, whilst the Y and X axes were abduction/adduction and long-axis rotation respectively. The Maya Graph Editor was used to visualize kinematics versus time graphs, measuring the XYZ rotations and translations for each joint, allowing for the analysis of movements over time and comparisons between each treatment.

For the purposes of this experiment, I specifically focused on the rotation about the Z-axis, representing flexion and extension, whilst the Y and X axes were abduction/adduction and long-axis rotation respectively, but were not measured here. To remove high-frequency noise (due to digitising or calibration errors) in the results, an average of the values across the duration the toe was held in max extension and flexion were taken.

Statistical analysis was carried out on the results using the software SPSS (Version 28.0.1.1). A Friedman test was done on the results to ascertain the statistical significance of changes in the Z-axis rotation of individual phalanges between treatments, with treatment being a within-subject factor and statistical significance being set at $P<0.05$.

Results

Overall, range of motion increased as soft tissues were removed – whilst removing integument had a slight, but statistically significant effect on ROM, removal of tendons had a much larger significant effect on ROM values.
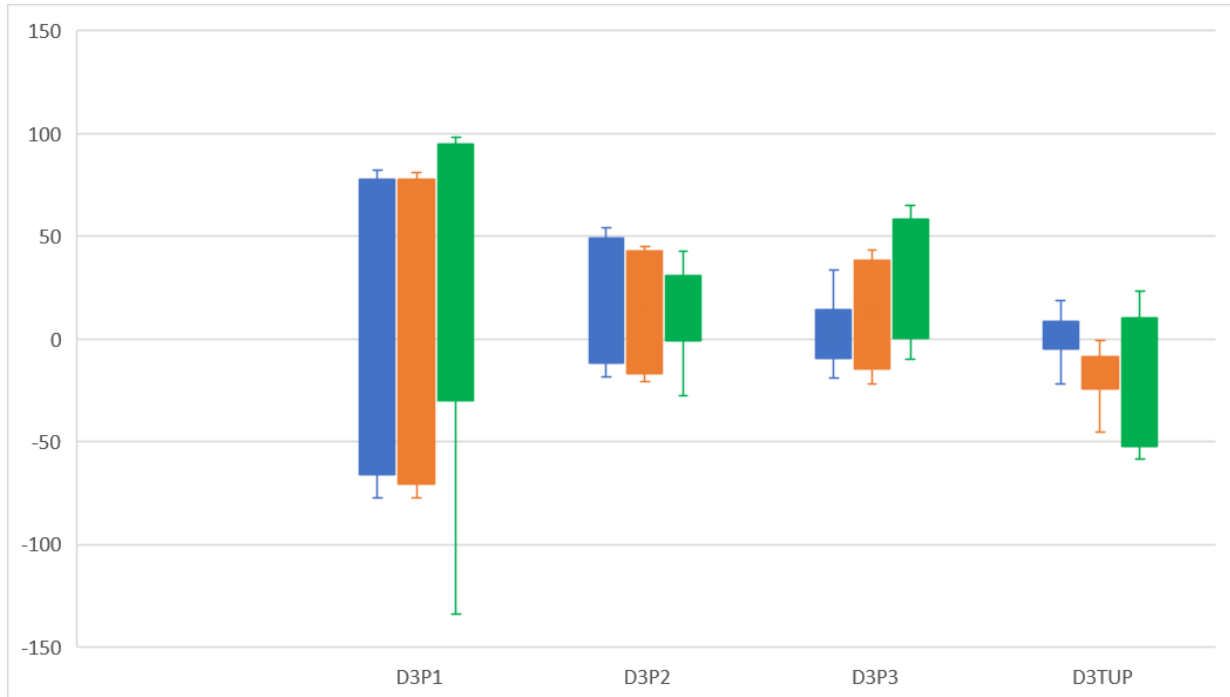
Figure 4.6 - Overall ROM (in degrees) for all phalanges with whiskers representing the minimum (max flexion) and maximum (max extension) values. D3P1 (digit 3, phalange 1), D3P2 (digit 3, phalange 2), D3P3 (digit 3, phalange 3) and D3TUP (digit 3 claw). Skin-on (blue), skin-off (orange) and tendons (green)

Digit 3	Number of frames		Extension	Flexion	Range
D3P1	**1336**	Skin-On	**77.68 (±2.331)**	**-70.97 (± 3.91)**	**148.65**
	1307	Skin-Off	81.02 (±1.55)	-73.42 (±2.78)	154.44
	416	Tendons	70.72 (±2.13)	-110.52 (±0.63)	181.24
D3P2	1348	Skin-On	47.67 (±2.87)	-13.2 (±2.7)	60.88
	1317	Skin-Off	39.77 (±1.38)	-13.96 (±4.11)	53.73
	417	Tendons	57.76 (±5.05)	-25.2 (±1.51)	82.96
D3P3	1337	Skin-On	27.58 (±3.64)	-13.46 (±2.58)	41.04
	1317	Skin-Off	34.96 (±2.79)	-16.26 (±2.01)	51.22
	416	Tendons	70.85 (±2.96)	-14.82 (±2.78)	85.68
D3TUP	564	Skin-On	15.42 (±1.51)	-9.75 (±1.93)	24.12
	1307	Skin-Off	-12.89 (±1.71)	-36.91 (±4.22)	49.8
	251	Tendons	30.55 (±3.87)	-52.55 (±3.27)	83.1

Table 4.1 - Max flexion/extension values (in degrees) for all phalanges at each treatment, along with total ROM (in degrees). Numbers in brackets are standard deviations of max flexion/extension values over duration. D3P1 – digit 3, phalange 1, D3P2 – digit 3, phalange 2, D3P3 – digit 3, phalange 3, D3TUP – digit 3 claw.

Digit 3, phalange 1

The ROM data for digit 3, phalange 1 was assessed for normality. The Shapiro-Wilk test indicated that the results were not normally distributed, $W (1336) = .813$, $p = <0.01$ for skin-on, $W (1307) = .776$, $p = <0.01$ for skin-off and $W (416) = .660$, $p = <0.01$ for tendons.

There was a statistically significant increase in ROM in digit 3 phalange 1 when soft tissues were removed, $\chi2(2) = 97.659$, $p = <0.01$. Post hoc analysis with Wilcoxon signed-rank tests was conducted with a Bonferroni correction applied, resulting in a significance level set at $p < 0.017$. Median (IQR) ROM for the skin-on, skin-off and tendons trials were 35.84 (-61.97 to 76.06), 33.92(-68.39 to 76.4) and 83.40 (4.29 to 93.26) respectively. There was a significant increase between the skin-on and skin-off trials (Z = 8.02, p = <0.01), but no significant increase between the skin-off and tendons trials (Z = 1.40, p = <1.60).

Removal of integument had little effect on ROM in digit 3, phalange 1 (an increase of only 5.78 degrees) compared to removing underlying musculature (an increase of 27.8 degrees).

Removing integument had little effect on extension ROM in digit 3, phalange 1, with a slight increase of 3.24 degrees between the skin-on and skin-off treatments and a slight increase of 2.45 degrees for extension. For flexion, ROM increased quite dramatically between the skin-off and tendons treatments (-37.1 degrees), whilst for extension, ROM decreased by 10.3 degrees.

Digit 3, phalange 2

The normality of ROM data for digit 3, phalange 2 was assessed and a Shapiro-Wilk test indicated that the results were not normally distributed, $W (1348) = .823$, $p = <0.01$ for skin-on, $W (1317) = .790$, $p = <0.01$ for skin-off and $W (416) = .779$, $p = <0.01$ for tendons.

There was a statistically significant increase in ROM in digit 3 phalange 2 when soft tissues were removed, $\chi2(2) = 136.98$, $p = <0.01$. Post hoc analysis with Wilcoxon signed-rank tests was conducted with a Bonferroni correction applied, resulting in a significance level set at $p < 0.017$. Median (IQR) ROM for the skin-on, skin-off and tendons trials were 25.80 (-9.28 to 47.35), 27.25 (-8.55 to 46.50)

and 23.69 (8.15 to 26.5834) respectively. There was a significant increase between the skin-on and skin-off trials (Z = 4.097, p = <0.01) and between the skin-off and tendons trials (Z = 16.44, p = <0.01).

ROM in digit 3, phalange 2 was slightly decreased by the removal of integument (a decrease of 7.15 degrees between the skin-on and skin-off treatments) compared to the removal of underlying musculature, which increased ROM (an increase of 29.2 degrees between the skin-on and tendons treatments).

For extension ROM in digit 3, phalange 2, the removal of integument had only a slight effect with a decrease of 7.9 degrees between the skin-on and skin-off treatments and an increase of only -0.76 degrees for flexion. For flexion, ROM increased between the skin-off and tendons treatments (-11.24 degrees), whilst for extension, ROM increased by 17.99 degrees.

Digit 3, phalange 3

A Shapiro-Wilk test indicated that the ROM data for digit 3, phalange 3 was non-normally distributed, W (1337) = .941, p = <0.01 for skin-on, W (1317) = .917, p = <0.01 for skin-off and W (416) = .756, p = <0.01 for tendons.

There was a statistically significant increase in ROM in digit 3 phalange 3 when soft tissues were removed, $\chi2(2)$ = 317.66, p = <0.01. Post hoc analysis with Wilcoxon signed-rank tests was conducted with a Bonferroni correction applied, resulting in a significance level set at p < 0.017. Median (IQR) ROM for the skin-on, skin-off and tendons trials were 2.93 (-9.38 to 13.98), 9.91 (-3.87 to 32.76) and 54.07 (.6421 to 58.41), respectively. There was a significant increase between the skin-on and skin-off trials (Z = 22.64, p = <0.01) and between the skin-off and tendons trials (Z = -3.00, p = 0.03).

Removing integument had a slight positive effect on ROM in digit 3, phalange 3 (an increase of 10.18 degrees between the skin-on and skin-off treatments) compared to removing underlying musculature (an increase of 34.46 degrees between the skin-off and tendons treatments).

Removing integument had little effect on ROM in digit 3, phalange 3, with an increase of 7.38 degrees of extension between the skin-on and skin-off treatments and an increase of only -2.8 degrees for flexion. For extension, ROM increased quite dramatically between the skin-off and tendons treatments (35.89 degrees), whilst for extension, ROM decreased by 5.39 degrees.

Digit 3 claw

A Shapiro-Wilk test on the digit 3 claw indicated that the results were not normally distributed, W (1317) = .977, p = <0.01 for skin-on, W (1307) = .930, p = <0.01 for skin-off and W (251) = .787, p = <0.01 for tendons.

There was a statistically significant increase in ROM in digit 3 phalange 3 when soft tissues were removed, $\chi2(2)$ = 263.434, p = <0.01. Post hoc analysis with Wilcoxon signed-rank tests was conducted with a Bonferroni correction applied, resulting in a significance level set at p < 0.017. Median (IQR) ROM for the skin-on, skin-off and tendons trials were 2.35 (-4.75 to 8.48), -13.59 (-24.16 to -8.95) and -.45 (-52.42 to 10.23), respectively. There was a significant increase between the skin-on and skin-off trials (Z = 16.44, p = <0.01) and between the skin-off and tendons trials (Z = 3.90, p = <0.01).

The ROM of the digit 3 claw was largely unaffected by the removal of integument (a decrease of 0.1 degrees between the skin-off and skin-on treatments) compared to the removal of underlying musculature (an increase of 59.08 degrees between the skin-off and tendons treatments).

However, removing integument had a dramatic effect on extension ROM in the digit 3 claw, with a decrease of 28.31 degrees between the skin-on and skin-off treatments and an increase of -27.16 degrees for flexion. In addition, the removal of underlying musculature increased extension ROM quite dramatically (43.44 degrees between the skin-off and tendons treatments), whilst for flexion, ROM increased by -15.64 degrees.

Discussion

Overall, the progressive removal of soft tissue led to an increase in the ROM of an ostrich foot. These results concur with previous studies (Hutson and Hutson 2012; White et al, 2016)) that the presence of soft tissues acts to significantly restrict ROM.

However, the results showed considerable variation in ROM between the phalanges, with overall ROM decreasing in the more distal phalanges relative to the more proximal ones. A possible cause for this variation might be differences in the level of soft tissue covering between individual phalanges. Digit 3, phalange 1 had the thickest layer of soft tissue and displayed the greatest increase in ROM as soft tissues were removed.

Similarities/differences between treatments

The removal of integument was found to have a smaller, but significant effect on overall ROM compared to the removal of underlying musculature, with small differences in ROM between the skin-on and skin-off treatments. This suggests that the presence of integument has only a slight effect on ROM. Conversely, there was a much larger significant increase in ROM between the skin-off and tendons treatments, suggesting that that the presence of underlying musculature has a greater effect on ROM.

A possible reason for this is due to the presence of thick layers of soft tissue (integument, muscles, fatty digit pads) that impair ROM in the ostrich foot. These layers of soft tissue provide an important role in shock absorption and energy storage during fast locomotion in the highly cursorial ostrich (Li et al 2017).

Similarities/differences between the individual phalanges

The range of motion for D3P1, throughout all three treatments, was much higher than the other three phalanges, with ROM decreasing in the more distal phalanges. A possible reason for a greater ROM in D3P1, is that that the metatarsophalangeal joint (which articulates between D3P1 and the tarsometatarsus) plays a major role in energy storage and release during fast locomotion (Li et al, 2017) in the highly cursorial ostrich, with the presence of various ligaments and tendons used in elastic energy generation.

Additionally, D3P1 displayed the greatest increase in ROM at progressive levels of dissection, principally due to the fact that this phalange had a thicker layer of soft tissue surrounding it than the other phalanges. The reason for this is the presence of the thick metatarsophalangeal pad leading to an elevation of the metatarsophalangeal joint above ground which further enhances elastic shock absorption during fast locomotion (Zhang et al, 2016). In particular, D3P1 displayed greater increase in flexion compared to extension between the skin-off and tendons treatments, due to the presence of the metatarsophalangeal pad leaving D3P1 slightly flexed in the reference pose.

Conversely, in both D3P2 and D3P3 (especially the latter), extension underwent a greater increase than flexion between the skin-off and tendons treatments. A reason for the greater effect on extension, as opposed to flexion, in these phalanges is that there was a thicker layer of soft tissue

surrounding the phalanges ventrally, as opposed to dorsally, leaving the phalange more extended in the reference pose. The thicker layer of ventral soft tissue is due to the presence of the fatty plantar pads underneath the phalange, which serve to provide a greater degree of shock absorption during high-speed locomotion.

The D3 claw had the lowest ROM on all phalanges when soft tissues were present (in both the skin-on and skin-off treatments). A possible reason for this could be because the D3 claw is a rigid element in the toe and functions both to provide forces at push-off and as a positional anchor at fast speed (Li et al, 2017).

Limitations of motion data

It is important to note that the quality of the motion data was comparatively poor, especially compared to the LEGO wand data from the previous chapter, with a great deal of high frequency noise in the max extension/flexion figures (see Figure 4.7):
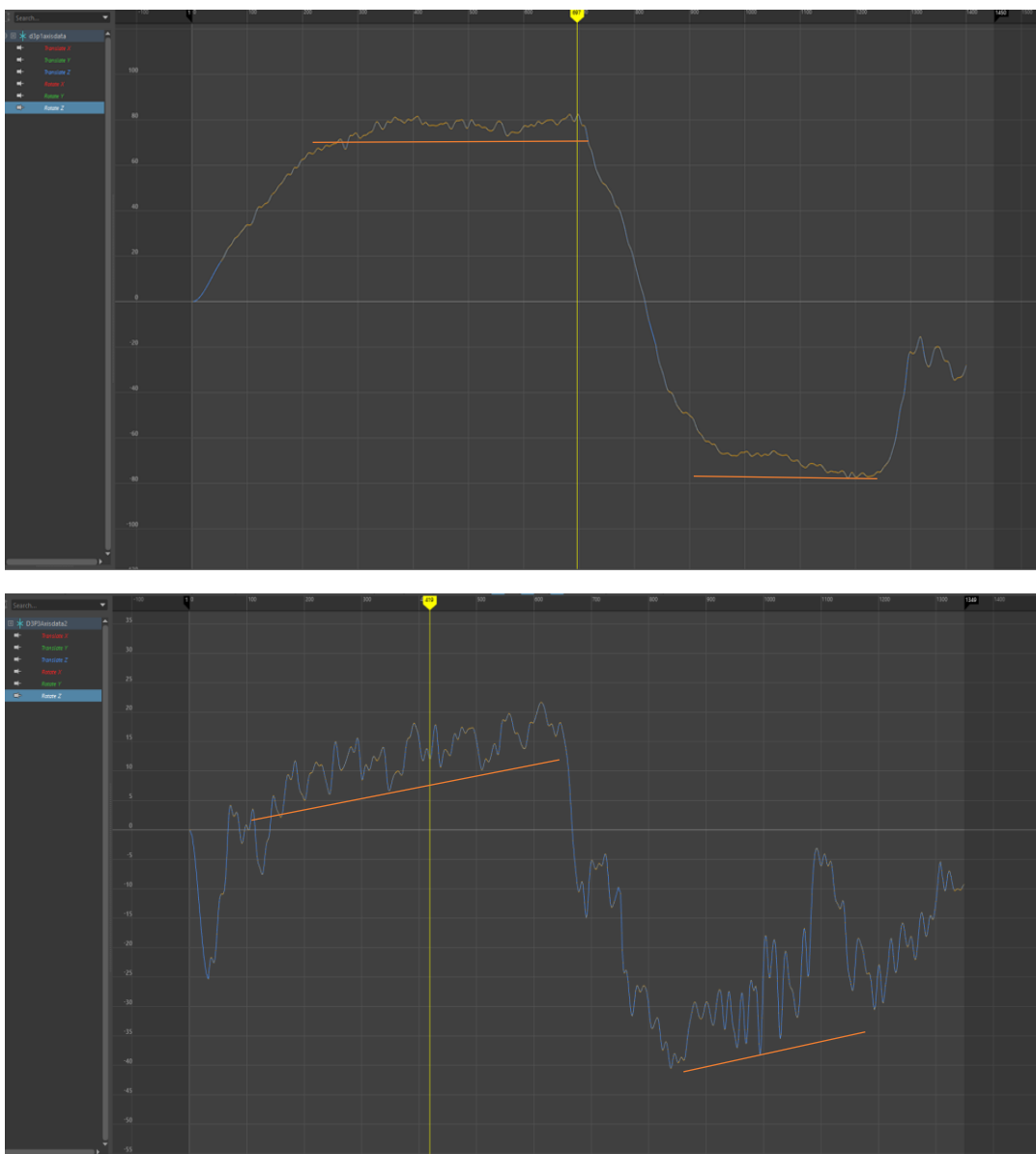
Figure 4.7 - Sample graphs of motion data recorded in Maya. Fig 7a) – Rotation z for flexion and extension motions for D3P1 skin-on (which had the least "noise"). Fig 7b) – Rotation around the z-axis D3P3 skin-off (which had the most "noise"). Areas of max extension/flexion (where average was taken, indicated by orange lines.

51

A likely reason for this variability could be a lack of marker retention throughout the experiment – several markers fell out both during dissection and the manipulations. This was a consequence of the great difficulty of applying the markers, due to the phalanges being difficult to get to because of the thickness of the skin and muscle tissue and cartilage making it difficult to ascertain whether a marker was actually in the bone.

A similar, but related issue was markers moving during dissection, due to the above-mentioned factors. For example, marker 11 (D3P1) changed position slightly during the manipulations for the tendons trial (see figure 4.8), which necessitated the bone model for D3P1 in Maya to be manually rotoscoped. In addition, the issue of markers falling out during skeletonization led to a great degree of subjectivity when it came to aligning the bones in the reference pose in Maya, as it had to be based on the approximate position of the few remaining markers with the photogrammetric model of the foot. This lack of objectivity resulted in the bones being slightly misaligned in the reference pose (see figure 4.8)
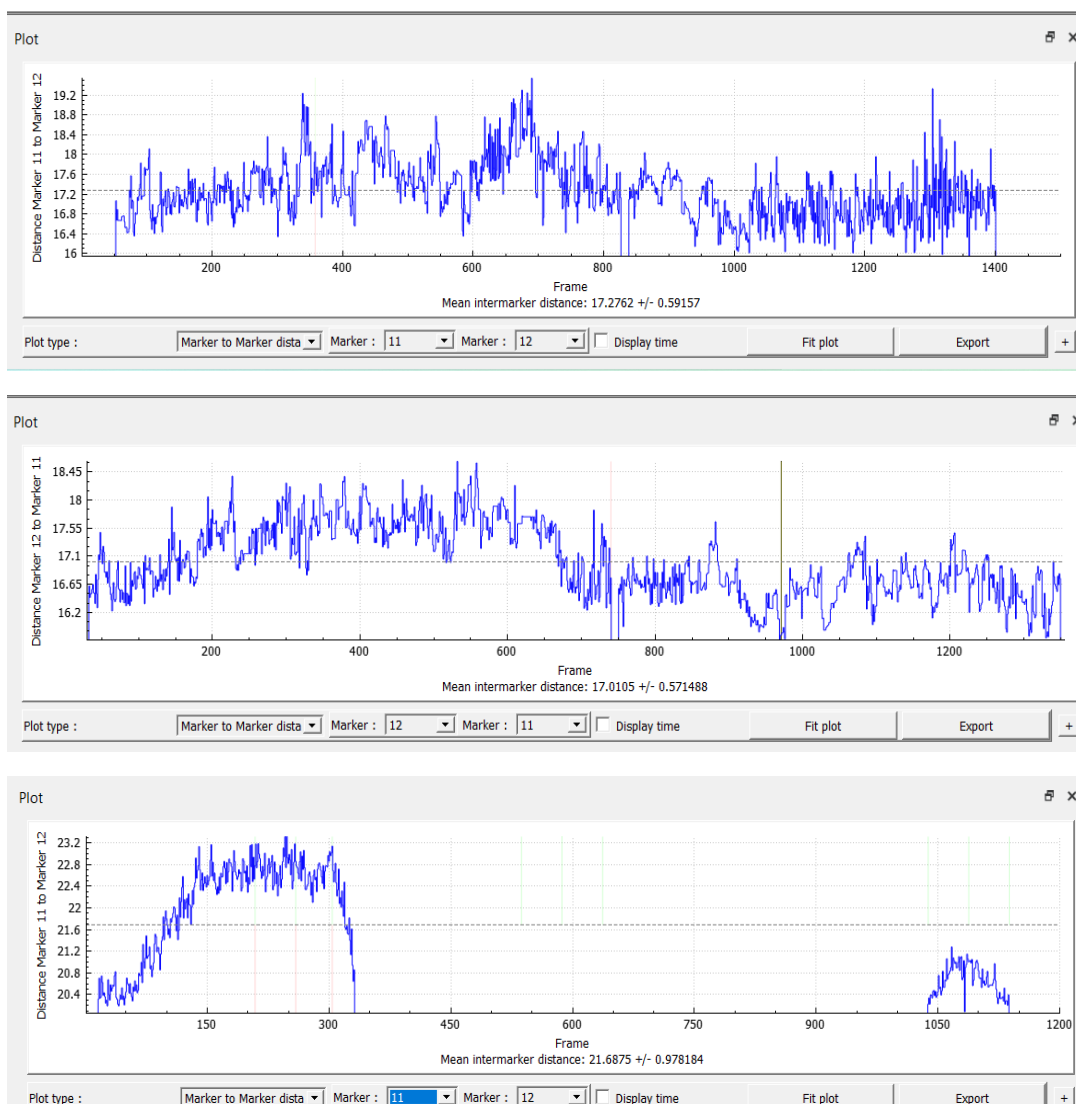
Figure 4.8 – Intermarker distances between markers 11 and 12 in skin-on (top), skin-off (middle) and tendons (bottom). In the tendons treatment, marker 11 moved during the manipulations – note the differences in accuracy (21.68 compared to 17.27 and 17.01 for the other two) and precision (0.98 compared to 0.59 and 0.57 for the other two) in the bottom figure. Intermarker distance is not visible for most of bottom plot due to a small amount of footage for flexion where the markers were visible.
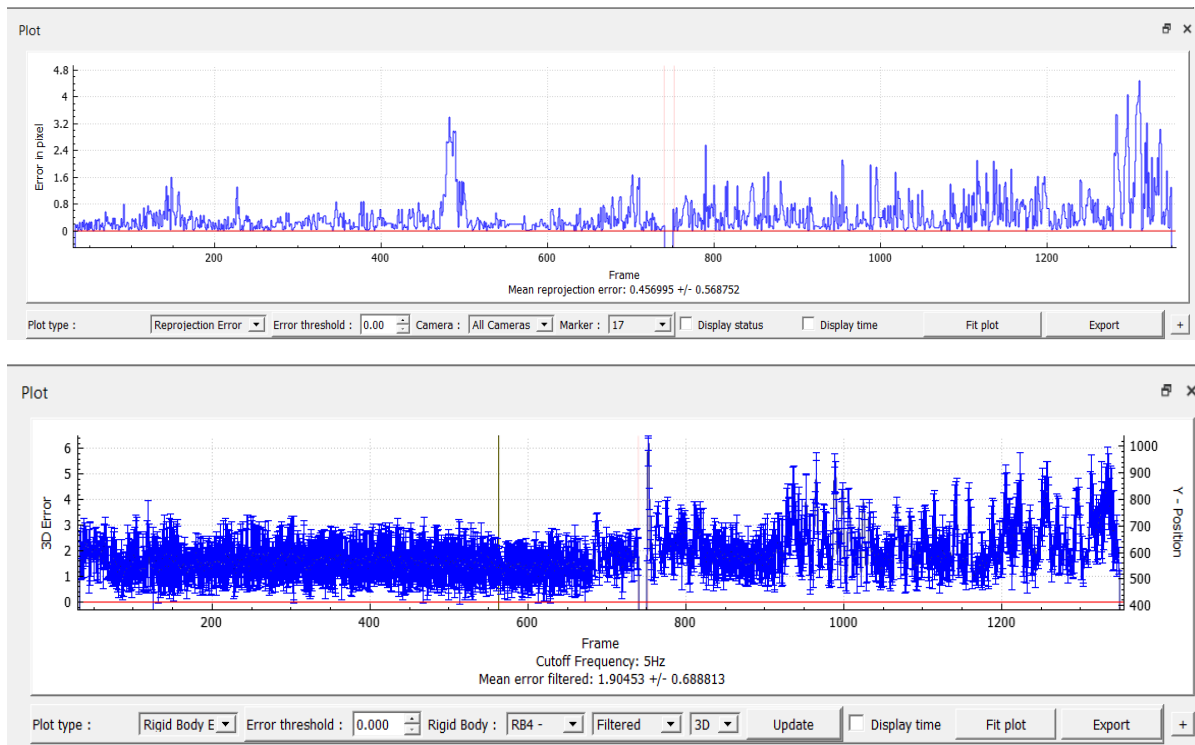
Figure 4.9 – Sample reprojection error (for marker 17 of the trial) and rigid body error graphs (for RB4 of the trial) – note the unevenness on both graphs, due to manual errors made during marker tracking.

The scaling of the photogrammetric models may have also contributed to this unevenness. Though efforts were made to ensure photogrammetric models were accurately scaled based on a scale bar within the photogrammetric model, small errors here could have affected marker coordinates so as to introduce error to calculated rigid body transformations. This effect was likely much smaller than that of moving or missing markers.

Conclusion

Whilst the workflow has the potential to be used effectively on biological data, it is clear, as indicated by the errors in the motion data detailed above, that the workflow is in need of a considerable deal of refinement needed before it can be considered truly effective. It may be that the expertise, or at least manual intervention, required offsets the affordability of the system.

For my second aim, it can be concluded that the removal of soft tissues led to an overall increase in ROM in an ostrich foot, as might be expected. However, the details of how ROM changes as soft tissue are removed, and how this varies between different bones in the toe are interesting. Overall ROM was highest in digit 3, phalange 1 and decreased in the more distal phalanges. Removal of integument was found to have a lesser impact on ROM than removal of underlying musculature for all phalanges, suggesting that it is underlying musculature that has the greater relevance for pedal ROM. The fatty tissue of the digit pads reduced flexion ROM in the more proximal phalanges. These results support previous conclusions that the presence of soft tissues significantly restricts ROM , meaning that the reconstruction of ROM in extinct animals, from their bones alone, requires an extensive knowledge of ROM in modern analogues.

5   Discussion

In this study, I have presented a low cost, comparatively easy-to-use workflow that applies marker-based XROMM methods using motion data from standard light-video cameras. In order to validate the workflow's quality, it is important to ascertain three things – 1) The system's ability to maintain marker-based XROMM's ability to produce accurate and precise results with ideal conditions, 2) demonstrate whether it can be used effectively on biological data in a case study and 3) identify potential pitfalls and possible areas for improvement.

Experimental set-up and workflow

The total hardware cost for the experimental setup, as described in Chapter 2, and used in Chapters 3 and 4, was less than £550 (not counting the laptop computer used for data analysis or the camera used for photogrammetry), with two comparatively inexpensive GoPro cameras (£270 each) used to collect video footage and a calibration object made of LEGO bricks (< £5). Photogrammetry was carried out using a Sony NEX-6 digital camera (£500), but could have been done with any camera (including one of the GoPros). All the software used in this workflow is inexpensive or free. Only the photogrammetry software Agisoft Metashape had a cost ($59), but equally capable open-source alternatives are available. For the most part, the workflow was easy-to-use, whilst being able to produce high-quality results.

It is important to note here that there is a degree of flexibility with aspects of the workflow. Whilst video data was collected using GoPro Black Hero 7 cameras and images for photogrammetry were collected using a Sony NEX-6 digital camera, the workflow is hypothetically compatible with any brand of camera – including smartphone cameras and Raspberry PI and Arduino camera modules Indeed, early in this project I started out using Raspberry PI cameras, but networking and synchronization complications resulted in a transition to GoPro cameras. GoPro cameras were used for this study because they are relatively inexpensive and can provide high picture quality at a wide range of settings, whilst the Sony NEX-6 was used due to its ability to provide a high picture quality.

Whilst Metashape was chosen for 3D modelling due to it being easy to use, relatively low cost ($59 for an academic license) and because it does not require a Nividia graphics card to function, the workflow is compatible with any photogrammetry software that can produce 3D digital models from photographs. The major open-source alternatives to Metashape are Colmap and Meshroom. Whilst Meshroom has a very intuitive interface and extremely customisable parameters, it requires an Nvidia graphics card to function, processing can be quite time-consuming and changing parameters may be complicated for new users and, whilst Colmap does not require an Nvidia graphics card. It can be complicated to use at times. Laser scanning, or even CT scanning could of course be used to digitize specimens, though these methods are expensive and somewhat defy the point of the low-cost setup.

Effectiveness of workflow

In Chapter 3, I to assessed whether the workflow could maintain marker-based XROMM's ability to produce highly accurate and precise results. For the context of this discussion, accuracy is defined as the intermarker distance recovered in XMALab (relative to the real distance) and precision is defined as the standard deviation of the intermarker distance (as defined in Knorlein et al, 2016).

The effect of differing camera settings (e.g., differences in resolution, framerate and field of view), as well as differing calibration positions, on accuracy and precision, in order to test the versatility of the

setup, and the effects of changes in field-of-view on within-frame accuracy (how accuracy varies across a single frame) were also assessed.

The results found that the setup could produce results in XMALab with a high degree of accuracy and precision overall. For the 2.7k/60 configuration (the most accurate), the accuracy for the horizontal distance was -0.0157mm, with a precision of 0.68mm, and the accuracy for the vertical distance was 0.0538mm, with a precision of 0.15mm.

Comparison of different camera settings revealed that accuracy and precision remained high, even when the resolution and framerate were changed (and when the calibration object was placed in differing positions).

However, changing field of view led to a substantial decrease in accuracy and precision (see chapter 3, figs. 3.7 and 3.8) – with the accuracy for the horizontal distance in wide-angle being -3.77mm, with a precision of 0.98 mm and the vertical distance being -0.91mm, with a precision of 0.43 and -2.11 mm, with a precision of 0.99mm and the vertical distance being -0.94mm, with a precision of 0.53mm in super-view. This is due to a greater amount of distortion in the images, which has been known to negatively affect accuracy and precision in XROMM studies (Brainerd et al, 2010).

Changing field of view also affected within-frame accuracy quite drastically, with the settings being most consistent and accurate in the linear, due to a reduced degree of distortion, and reducing in wide-angle and super-view. In all three settings, accuracy was highest at the centre of the frame. (see chapter 3, figure 9).
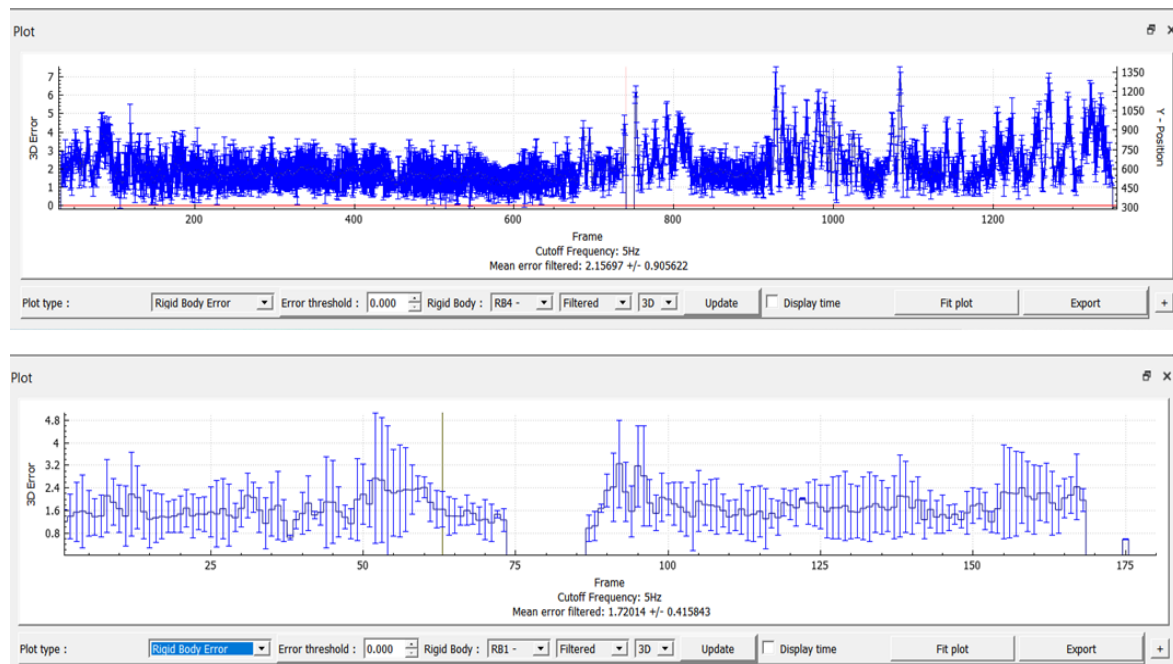
Figure 5.4 – Rigid body errors for LEGO wand (above) and D3P3 for skin-off trial (below) – note both the higher absolute mean error (2.15697) and standard error (0.905622) for the ostrich data compared to the LEGO wand (1.72014 mean error and 0.415843 standard error).

Another factor that had to be demonstrated is the workflow's possible effectiveness on biological data. In order to ascertain this, an ostrich (*Struthio camelus*) foot was dissected and pedal ROM recorded at each progressive level of dissection. Whilst the results (see chapter 4) indicate that the workflow has the potential to be used effectively on biological data, it can also be concluded that

there are many possible areas of improvement needed before it can be considered truly effective for use on biological data.

This can be concluded from the limitations in the results from the *Struthio* foot, mostly stemming from the comparatively poor quality of the motion data, which had a great deal of high-frequency noise seen in the max extension/flexion figures. In addition, a comparison of the rigid body errors of the biological data RBTs (rigid body transformations, with those of the LEGO wand, found that the RBTs for the LEGO wand had a lower rigid body error (both absolute mean and standard error) than for the ostrich data (see fig. 5.1).

There were many causes for this unreliability, with factors including a lack of marker retention (markers moving or falling out during the manipulations and during skeletonisation), manual errors made during marker tracking (due to markers blending in with the ostrich foot) and a possible lack of uniformity in the scaling of photogrammetric models (see chapter 4 for more detail).

From all these observations, it can be concluded that, whilst the workflow maintains marker-based XROMM's ability to produce accurate and precise results and (and can do so at a variety of different camera settings, increasing its versatility) and has the potential to be used in an effective way on biological data, it is also in need of a considerable deal of refinement before it can be considered truly effective. However, it should be noted that XROMM workflows suffer similar issues – that optimal scenarios can produce excellent accuracy and precision, but the realities of working with biological data mean that there will always be difficulties with marker insertion, tracking, and reconstruction.

ROM in a *Struthio* foot and its inferences for fossil archosaurs

The analysis of the *Struthio* foot concluded that overall ROM was increased with the progressive removal of soft tissue, with considerable variation between individual phalanges, possibly due to differing levels of soft tissue covering – with ROM being the highest in phalange 1 (which had the thickest layers of soft tissue surrounding it) and decreasing in the more distal phalanges.

These results support previous conclusions (White et al, 2016; Hutson and Hutson, 2013) that the presence of soft tissues significantly restricts joint ROM. In particular, the removal of integument was also shown to have little effect on overall pedal ROM in the ostrich foot compared to the removal of underlying musculature. This is similar to the conclusions of previous studies on archosaur finger joint ROM (Hutson and Hutson, 2015; Hutson and Hutson, 2018) and elbow ROM (Hutson and Hutson 2013), which also concluded that the removal of underlying musculature had a greater effect on ROM than integument.

The results from the ostrich data have important implications for reconstructions of pedal ROM in bipedal fossil archosaurs and further indicates the need for extensive knowledge of ROM in modern analogues to be considered when reconstructing the movements of fossil taxa.

Ostriches are among the most cursorial of living birds – being recognised as the fastest extant bipeds (Schaller et al, 2009) with the highest capacity for long endurance-running (Alexander et al, 1979). Accordingly, adaptations for fast locomotion are seen in multiple aspects of ostrich foot morphology, e.g., reduction of number of toes; permanently elevated metatarsophalangeal joints (Li et al 2017; Schaller et al, 2011).

Many aspects of the ROMs reported in the ostrich foot, especially the similarities and differences seen between the individual phalanges, can be explained in the light of adaptations for high cursoriality. For instance, digit 3 phalange 1 had the highest ROM compared to the more distal

phalanges due to the role of the metatarsophalangeal joint (and various ligaments and tendons used in elastic energy storage) in energy storage and release (Li et al, 2017) during high-speed locomotion, and the D3 claw had the lowest ROM with soft tissues attached because it serves as a rigid element to provide forces at push-off and serve as a positional anchor during high-speed locomotion (Schaller et al, 2011).

These results confirm that soft tissue reconstructions of pedal ROM in fossil taxa, based on both extant analogues and osteological correlates of soft tissue on fossil remains, could be used to aid researchers in assessing degrees of cursoriality in fossil bipedal archosaurs. This has important implications for reconstructing aspects of their locomotion, behaviours and palaeoecology. Whilst comparisons of pedal ROM in a broader range of avian taxa (including other ratites), including cursorial and non-cursorial taxa, might be useful in this regard, that is beyond the scope of this study.

Pitfalls and potential areas for improvement

This workflow is not without its pitfalls. Initial attempts at using Raspberry PI microcomputers to capture video footage were hampered by repeated technical difficulties (cameras frequently developing faults, network synchronization failing, low resolutions and framerates) which spurred a switch to GoPro Hero 7 Black cameras. Similarly, issues with picture quality necessitated a switch from a Sony camera to the Sony NEX-6. As well as this, frequent issues with model quality, as well as lengthy processing time, in Meshroom necessitated a shift to Metashape, which offered both better-quality models and a faster processing time.

As well as this, the affordability of the system may be offset by the intensive file management that the workflow requires – since the synchronisation of video data has to be done manually, the synchronising, trimming and managing of files can often be time-consuming. At the end of the ostrich dataset, I ended up with roughly 18 files in total (the raw data, the synchronised footage, the Blender file, the photogrammetric models of each phalange (roughly in total) and the Maya integration scene).

Another potential flaw of the workflow is that due to object opacity, camera view of markers can be quite limited. In the experiment, the cameras were placed 45 degrees to each other, leading to the possibility that individual markers may have not been detected. Hypothetically, the addition of a third camera or a change in camera position might increase the reliability of the results.

When considering optimal camera settings, slight trade-offs were encountered between accuracy, precision and reprojection error when considering optimum framerate, field of view and resolution. It is important to note that the linear field of view, due to the lesser degree of distortion, produced the most accurate and precise results.

For biological data, care must be taken with aspects of marker choice and placement, particularly when performing studies on smaller, more delicate bones (e.g. chicken bones). This was shown in early attempts at collecting biological data using chicken (*Gallus gallus domesticus*) specimens were repeatedly hampered due to a lack of marker retention, brought on by the need to compromise marker retention with avoiding bone breakage.

As well as this, a lack of marker retention complicated multiple aspects of data analysis for the dissection trial. During skeletonisation of the *Struthio* foot, some of the nails that I had used as markers fell out, necessitating the creation of "virtual markers" made using a pre-dissection photogrammetric model of the *Struthio* foot and placing locators based on the approximate

locations of the missing markers (for more on this, see chapter 4). In addition, marker tracking was complicated by some of the markers moving during dissection.

A lack of marker retention also meant that alignment had to be manually adjusted via scientific rotoscoping (Gatesy et al, 2010) based on the position of the few remaining markers relating to a photogrammetric model of the foot. This led to a great degree of subjectivity in the alignment of the 3D models of the bones - this lack of objectivity meant that the bones were slightly misaligned in the reference pose (for instance, the claw was slightly raised). This meant that since the individual phalanges were aligned based on where they naturally rested, "zero" degrees rotation did not represent a mathematical alignment.

A possible means to improve marker retention would be to use specialist screws as markers and place them using a small screwdriver, possibly with pilot holes drilled into the bone. However, this would not be possible to use on smaller, more delicate bones (e.g. if a chicken were being studied) without incurring the risk of breaking them.

A related issue was the centres of some of the markers blending in with the colouration of the ostrich foot during dissection. This meant that there were unavoidable manual errors in marker tracking where markers could not be distinguished. This led to uneven RBTs (since different individual frames each had slightly different 2D co-ordinates – see figure 5.1) and bone models often having to be manually rotoscoped in Maya to align them to the camera's motions. A possible way to rectify this would be to find some way to make the centres of individual markers stand out – possibly by using Tippex to mark the centre of the marker.

Concluding remarks

The main conclusions of this study are:

- The setup cost less than £550 – not counting the laptop computer used for data analysis and the Sony NEX-6 camera used for photogrammetry.

- Whilst the system retained XROMM's ability to produce highly accurate and precise results at a variety of camera settings, peak accuracy and precision was seen at the 2.7kp/60fps/linear configuration – however, past a certain point, changing resolution did not significantly affect accuracy and precision.

- From dissection of the ostrich foot, it can be concluded that, whilst the workflow can potentially be used in an effective way on biological data, there is a great deal of refinement needed before it can be considered effective.

- Soft tissue removal in an ostrich foot was found to markedly increase the ROM – with considerable variation across the individual phalanges. This further reiterates the need for extensive ROM knowledge in extant analogues when reconstructing the movements of extinct taxa – and provides a possible framework by which researchers can assess degrees of cursoriality in fossil bipedal archosaurs.

My aim with this study was to demonstrate the effectiveness of a relatively low-cost, easy-to-use workflow for range of motion studies using two comparatively inexpensive GoPro cameras and easy-to-use, inexpensive software packages.

Through the use of a LEGO wand, I have demonstrated that this workflow maintains marker-based XROMM's ability to produce accurate and precise results and can do so at a variety of different camera settings. From dissecting an ostrich foot (*Struthio camelus*), I also showed that, whilst this

workflow has the potential be used in an effective way on biological data – however, there is still a great deal of refinement needed before it can be considered effective.

6   Bibliography

Alexander, R. M., Maloiy, G. M. O., Njau, R., & Jayes, A. S. (1979). Mechanics of running of the ostrich (Struthio camelus). Journal of Zoology, 187(2), 169-178.

Alonso, P. D., Milner, A. C., Ketcham, R. A., Cookson, M. J., & Rowe, T. B. (2004). The avian nature of the brain and inner ear of Archaeopteryx. Nature, 430(7000), 666.

Bakker, R. T. (1971). Ecology of the brontosaurs. Nature, 229(5281), 172-174.

Barrett, P. M., & Maidment, S. C. (2017). The evolution of ornithischian quadrupedality. Journal of Iberian Geology, 43(3), 363-377.

Bengtson, S., Cunningham, J. A., Yin, C., & Donoghue, P. C. (2012). A merciful death for the "earliest bilaterian," Vernanimalcula. Evolution & development, 14(5), 421-427.

Bennett, S. C. (1997). Terrestrial locomotion of pterosaurs: a reconstruction based on *Pteraichnus* trackways. Journal of Vertebrate Paleontology, 17(1), 104-113.

Bishop, P. J., Cuff, A. R., & Hutchinson, J. R. (2021). How to build a dinosaur: Musculoskeletal modeling and simulation of locomotor biomechanics in extinct animals. Paleobiology, 47(1), 1-38.

Bonnan, M. F. (2004). Morphometric analysis of humerus and femur shape in Morrison sauropods: implications for functional morphology and paleobiology. Paleobiology, 30(3), 444-470.

Bonnan, M. F. (2007). Were the basal sauropodomorph dinosaurs *Plateosaurus* and *Massospondylus* habitual quadrupeds?. Evolution and palaeobiology of early sauropodomorph dinosaurs, 139-155.

Bonnan, M. F., F. Matthew, and P. Senter. "Evolution and Palaeobiology of Early Sauropodomorph Dinosaurs. Special Papers in Palaeontology 77." (2007): 139-155.

Bonnan, M. F., Sandrik, J. L., Nishiwaki, T., Wilhite, D. R., Elsey, R. M., & Vittore, C. (2010). Calcified cartilage shape in archosaur long bones reflects overlying joint shape in stress-bearing elements: Implications for nonavian dinosaur locomotion. The Anatomical Record: Advances in Integrative Anatomy and Evolutionary Biology, 293(12), 2044-2055.

Bonnan, M. F., Shulman, J., Varadharajan, R., Gilbert, C., Wilkes, M., Horner, A., & Brainerd, E. (2016). Forelimb kinematics of rats using XROMM, with implications for small eutherians and their fossil relatives. PloS one, 11(3), e0149377.

Brainerd, E. L., Baier, D. B., Gatesy, S. M., Hedrick, T. L., Metzger, K. A., Gilbert, S. L., & Crisco, J. J. (2010). X-ray reconstruction of moving morphology (XROMM): precision, accuracy and applications in comparative biomechanics research. Journal of Experimental Zoology Part A: Ecological Genetics and Physiology, 313(5), 262-279.

Brocklehurst, R. J., Moritz, S., Codd, J., Sellers, W. I., & Brainerd, E. L. (2017). Rib kinematics during lung ventilation in the American alligator (*Alligator mississippiensis*): an XROMM analysis. Journal of Experimental Biology, 220(17), 3181-3190.

Brocklehurst, R. J., Moritz, S., Codd, J., Sellers, W. I., & Brainerd, E. L. (2017). Rib kinematics during lung ventilation in the American alligator (Alligator mississippiensis): an XROMM analysis. Journal of Experimental Biology, 220(17), 3181-3190.

Bryant, H. N., & Seymour, K. L. (1990). Observations and comments on the reliability of muscle reconstruction in fossil vertebrates. Journal of Morphology, 206(1), 109-117.

Camp, A. L., & Brainerd, E. L. (2015). Reevaluating musculoskeletal linkages in suction-feeding fishes with X-ray reconstruction of moving morphology (XROMM). Integrative and comparative biology, 55(1), 36-47.

Camp, A. L., Scott, B., Brainerd, E. L., & Wilga, C. D. (2017). Dual function of the pectoral girdle for feeding and locomotion in white-spotted bamboo sharks. Proceedings of the Royal Society B: Biological Sciences, 284(1859), 20170847.

Camp, A. L., & Brainerd, E. L. (2022). A new conceptual framework for the musculoskeletal biomechanics and physiology of ray-finned fishes. Journal of Experimental Biology, 225(Suppl_1), jeb243376.

Carpenter, K. (2002). Forelimb biomechanics of non-avian theropod dinosaurs in predation. Senckenbergiana lethaea, 82(1), 59-75.

Carpenter, K., & Smith, M. (2001). Forelimb osteology and biomechanics of Tyrannosaurus rex. Mesozoic vertebrate life, 90.

Carpenter, K., & Wilson, Y. (2008). A new species of *Camptosaurus* (Ornithopoda: Dinosauria) from the Morrison Formation (Upper Jurassic) of Dinosaur National Monument, Utah, and a biomechanical analysis of its forelimb. Annals of Carnegie Museum, 76(4), 227-264.

Cobley, M. J., Rayfield, E. J., & Barrett, P. M. (2013). Inter-vertebral flexibility of the ostrich neck: implications for estimating sauropod neck flexibility. PLoS One, 8(8), e72187.

Cunningham, J. A., Rahman, I. A., Lautenschlager, S., Rayfield, E. J., & Donoghue, P. C. (2014). A virtual world of palaeontology. Trends in ecology & evolution, 29(6), 347-357.

Das, A. J., Murmann, D. C., Cohrn, K., & Raskar, R. (2017). A method for rapid 3D scanning and replication of large paleontological specimens. PloS one, 12(7), e0179264.

Davies, T. G., Rahman, I. A., Lautenschlager, S., Cunningham, J. A., Asher, R. J., Barrett, P. M., ... & Braga, J. (2017). Open data and digital morphology. Proceedings of the Royal Society B: Biological Sciences, 284(1852), 20170194.

Demuth, O. E., Rayfield, E. J., & Hutchinson, J. R. (2020). 3D hindlimb joint mobility of the stem-archosaur Euparkeria capensis with implications for postural evolution within Archosauria. Scientific reports, 10(1), 1-14.

Deng, B. (2015). Motion studies: See how they run. Nature, 525(7567), 145-146.

Dilkes, D. W. (2001). An ontogenetic perspective on locomotion in the Late Cretaceous dinosaur Maiasaura peeblesorum (Ornithischia: Hadrosauridae). Canadian Journal of Earth Sciences, 38(8), 1205-1227.

Donoghue, P. C., & Purnell, M. A. (2009). Distinguishing heat from light in debate over controversial fossils. BioEssays, 31(2), 178-189.

Dzemski, G., & Christian, A. (2007). Flexibility along the neck of the ostrich (Struthio camelus) and consequences for the reconstruction of dinosaurs with extreme neck length. Journal of Morphology, 268(8), 701-714.

Falkingham, P. L. (2012). Acquisition of high-resolution three-dimensional models using free, open-source, photogrammetric software. Palaeontologia electronica, 15(1), 1-15.

Falkingham, P. L. (2013). Low cost 3D scanning using off-the-shelf video gaming peripherals. Journal of Paleontological Techniques, 11, 1-9.

Falkingham, P. L. 3D photogrammetry.

Falkingham, P. L., Bates, K. T., Avanzini, M., Bennett, M., Bordy, E. M., Breithaupt, B. H., ... & Belvedere, M. (2018). A standard protocol for documenting modern and fossil ichnological data. Palaeontology, 61(4), 469-480.

Falkingham, P. L., Maidment, S. C., Lallensack, J. N., Martin, J. E., Suan, G., Cherns, L., ... & Barrett, P. M. (2021). Late Triassic dinosaur tracks from Penarth, south Wales. Geological Magazine, 1-12.

Fau, M., Cornette, R., & Houssaye, A. (2016). Photogrammetry for 3D digitizing bones of mounted skeletons: Potential and limits. Comptes Rendus Palevol, 15(8), 968-977.

Gatesy, S. M., Baier, D. B., Jenkins, F. A., & Dial, K. P. (2010). Scientific rotoscoping: a morphology-based method of 3-D motion analysis and visualization. Journal of Experimental Zoology Part A: Ecological Genetics and Physiology, 313(5), 244-261.

Gatesy, S. M., Manafzadeh, A. R., Bishop, P. J., Turner, M. L., Kambic, R. E., Cuff, A. R., & Hutchinson, J. R. (2022). A proposed standard for quantifying 3-D hindlimb joint poses in living and extinct archosaurs. Journal of Anatomy.

Gishlick, A. D. (2001). The function of the manus and forelimb of *Deinonychus antirrhopus* and its importance for the origin of avian flight. Gauthier and Gall, 301-318.

Hatcher, J. B. (1901). *Diplodocus* (Marsh): its osteology, taxonomy, and probable habits, with a restoration of the skeleton (Vol. 1, No. 1-4). Carnegie institute.

Holliday, C. M., Ridgely, R. C., Sedlmayr, J. C., & Witmer, L. M. (2010). Cartilaginous epiphyses in extant archosaurs and their implications for reconstructing limb function in dinosaurs. PLoS One, 5(9), e13120.

Holliday, C. M., Ridgley, R. C., Sedlmayr, J. C., & Witmer, L. M. (2001, December). The articular cartilage of extant archosaur limb bones: implications for dinosaur functional morphology and allometry. In AMERICAN ZOOLOGIST (Vol. 41, No. 6, pp. 1473-1474). 1313 DOLLEY MADISON BLVD, NO 402, MCLEAN, VA 22101 USA: SOC INTEGRATIVE COMPARATIVE BIOLOGY.

Hutchinson, J. R., Anderson, F. C., Blemker, S. S., & Delp, S. L. (2005). Analysis of hindlimb muscle moment arms in *Tyrannosaurus rex* using a three-dimensional musculoskeletal computer model: implications for stance, gait, and speed. Paleobiology, 31(4), 676-701.

Hutson, J. D., & Hutson, K. N. (2012). A test of the validity of range of motion studies of fossil archosaur elbow mobility using repeated-measures analysis and the extant phylogenetic bracket. Journal of Experimental Biology, 215(12), 2030-2038.

Hutson, J. D., & Hutson, K. N. (2013). Using the American alligator and a repeated-measures design to place constraints on in vivo shoulder joint range of motion in dinosaurs and other fossil archosaurs. Journal of Experimental Biology, 216(2), 275-284.

Hutson, J. D., & Hutson, K. N. (2014). A repeated-measures analysis of the effects of soft tissues on wrist range of motion in the extant phylogenetic bracket of dinosaurs: Implications for the functional origins of an automatic wrist folding mechanism in Crocodilia. The Anatomical Record, 297(7), 1228-1249.

Jablonski, D., & Shubin, N. H. (2015). The future of the fossil record: Paleontology in the 21st century. Proceedings of the National Academy of Sciences, 112(16), 4852-4858.

Jannel, A., Nair, J. P., Panagiotopoulou, O., Romilio, A., & Salisbury, S. W. (2019). "Keep your feet on the ground": Simulated range of motion and hind foot posture of the Middle Jurassic sauropod Rhoetosaurus brownei and its implications for sauropod biology. Journal of morphology, 280(6), 849-878.

Karim, T. S., Burkhalter, R., Farrell, Ú. C., Molineux, A., Nelson, G., Utrup, J., & Butts, S. H. (2016). Digitization workflows for paleontology collections. Palaeontologia Electronica, 19(3), 1-14.

Knight, K. (2012). DINOSAUR RANGE OF MOTION STUDIES VINDICATED.

Knörlein, B. J., Baier, D. B., Gatesy, S. M., Laurence-Chasen, J. D., & Brainerd, E. L. (2016). Validation of XMALab software for marker-based XROMM. Journal of Experimental Biology, 219(23), 3701-3711.

Laurence-Chasen, J. D., Manafzadeh, A. R., Hatsopoulos, N., Ross, C., & Arce-McShane, F. (2020). Integrating XMALab and DeepLabCut for high-throughput XROMM. BioRxiv.

Lautenschlager, S. (2013). Cranial myology and bite force performance of *Erlikosaurus andrewsi*: a novel approach for digital muscle reconstructions. Journal of Anatomy, 222(2), 260-272.

Lautenschlager, S. (2016). Digital reconstruction of soft-tissue structures in fossils. The Paleontological Society Papers, 22, 101-117.

Lautenschlager, S., Rayfield, E. J., Altangerel, P., Zanno, L. E., & Witmer, L. M. (2012). The endocranial anatomy of Therizinosauria and its implications for sensory and cognitive function. PLoS One, 7(12), e52289.

Lebrun, R., & Orliac, M. J. (2016). Morphomuseum: an online platform for publication and storage of virtual specimens. The Paleontological Society Papers, 22, 183-195.

Maidment, S. C., & Barrett, P. M. (2012). Does morphological convergence imply functional similarity? A test using the evolution of quadrupedalism in ornithischian dinosaurs. Proceedings of the Royal Society B: Biological Sciences, 279(1743), 3765-3771.

Maidment, S. C., Bates, K. T., Falkingham, P. L., VanBuren, C., Arbour, V., & Barrett, P. M. (2014). Locomotion in ornithischian dinosaurs: an assessment using three-dimensional computational modelling. Biological Reviews, 89(3), 588-617.

Maiwald, C., Arndt, A., Nester, C., Jones, R., Lundberg, A., & Wolf, P. (2017). The effect of intracortical bone pin application on kinetics and tibiocalcaneal kinematics of walking gait. Gait & Posture, 52, 129-134.

Mallison, H., & Wings, O. (2014). Photogrammetry in palaeontology–a practical guide. Journal of Paleontological Techniques.

Manafzadeh, A. R., & Padian, K. (2018). ROM mapping of ligamentous constraints on avian hip mobility: implications for extinct ornithodirans. Proceedings of the Royal Society B: Biological Sciences, 285(1879), 20180727.

Manafzadeh, A. R., Kambic, R. E., & Gatesy, S. M. (2021). A new role for joint mobility in reconstructing vertebrate locomotor evolution. Proceedings of the National Academy of Sciences, 118(7).

Marsh, O. C. (1883). Principal characters of American Jurassic dinosaurs; Part VI, Restoration of *Brontosaurus*. American Journal of Science, (152), 81-85.

Marsh, O. C. (1896). The dinosaurs of North America (Vol. 16). US Government Printing Office.

Mukaddam, R., Bordy, E. M., Lockley, M. G., & Chapelle, K. E. (2021). Reviving *Kalosauropus*, an Early Jurassic sauropodomorph track from southern Africa (Lesotho). Historical Biology, 33(11), 2908-2930.

Murdock, D. J., Donoghue, P. C., Bengtson, S., & Marone, F. (2012). Ontogeny and microstructure of the enigmatic Cambrian tommotiid *Sunnaginia Missarzhevsky*, 1969. Palaeontology, 55(3), 661-676.

Nesbitt, S. J. (2009). The early evolution of archosaurs: relationships and the origin of major clades. Columbia University.

Nicholls, E. L., & Russell, A. P. Structure and function of the pectoral girdle and forelimb of. *Struthiomimus altus*, 643-677.

Olsen, A., Hernandez, P., Camp, A., & Brainerd, E. (2017). Linking morphology and motion: testing multibody simulations against in vivo cranial kinematics in suction feeding fishes using XROMM. The FASEB Journal, 31(1_supplement), 90-1.

Osborn, H. F., Wortman, J. L., & Knight, W. C. (1898). Additional characters of the great herbivorous dinosaur *Camarasaurus*. order of the Trustees, American Museum of Natural History.

Perez-De-La Fuente, R., Gehler, A., Farnum, C. W., & Farrell, B. D. (2019). Digitisation as a tool to promote transparency between collections: the case of the Baltic amber from the Königsberg collection at the Museum of Comparative Zoology. Spanish Journal of Paleontology, 34(1).

PERSONS IV, W. S., & Currie, P. J. (2012). Dragon tails: convergent caudal morphology in winged archosaurs. Acta Geologica Sinica-English Edition, 86(6), 1402-1412.

Rahman, I. A., & Lautenschlager, S. (2016). Applications of three-dimensional box modeling to paleontological functional analysis. The Paleontological Society Papers, 22, 119-132.

Rahman, I. A., & Smith, S. Y. (2014). Virtual palaeontology: computer-aided analysis of fossil form and function. Journal of Paleontology, 88(4), 633-635.

Rayfield, E. J. (2007). Finite element analysis and understanding the biomechanics and evolution of living and fossil organisms. Annu. Rev. Earth Planet. Sci., 35, 541-576.

Romano, M., Antonelli, M., Palombo, M. R., Rossi, M. A., & Agostini, S. (2021). Drone testing for 3D reconstruction of massive mounted skeletons in museums: the case of *Mammuthus meridionalis* (Nesti 1825) from Madonna della Strada (Scoppito, L'Aquila, Italy). Historical Biology, 1-10.

Romer, A. S. (1927). The pelvic musculature of ornithischian dinosaurs. Acta Zoologica, 8(2-3), 225-275.

Rücklin, M., Donoghue, P. C., Johanson, Z., Trinajstic, K., Marone, F., & Stampanoni, M. (2012). Development of teeth and jaws in the earliest jawed vertebrates. Nature, 491(7426), 748.

Schaller, N. U., Herkner, B., Villa, R., & Aerts, P. (2009). The intertarsal joint of the ostrich (Struthio camelus): anatomical examination and function of passive structures in locomotion. *Journal of anatomy*, *214*(6), 830-847.

Schaller, N. U., D'Août, K., Villa, R., Herkner, B., & Aerts, P. (2011). Toe function and dynamic pressure distribution in ostrich locomotion. *Journal of Experimental Biology*, *214*(7), 1123-1130.

Schmidt, D. N., Rayfield, E. J., Cocking, A., & Marone, F. (2013). Linking evolution and development: Synchrotron Radiation X-ray tomographic microscopy of planktic foraminifers. Palaeontology, 56(4), 741-749.

Schwarz, D., Wings, O., & Meyer, C. A. (2007). Super sizing the giants: first cartilage preservation at a sauropod dinosaur limb joint. Journal of the Geological Society, 164(1), 61-65.

Senter, P. (2005). Function in the stunted forelimbs of *Mononykus olecranus* (Theropoda), a dinosaurian anteater. Paleobiology, 31(3), 373-381.

Senter, P., & Parrish, J. M. (2006). Forelimb function in the theropod dinosaur *Carnotaurus sastrei*, and its behavioural implications. PaleoBios, 26(3), 7-17.

Shubin, N. H., Daeschler, E. B., & Jenkins Jr, F. A. (2006). The pectoral fin of *Tiktaalik roseae* and the origin of the tetrapod limb. Nature, 440(7085), 764.

Stevens, K. A., & Parrish, J. M. (1999). Neck posture and feeding habits of two Jurassic sauropod dinosaurs. Science, 284(5415), 798-800.

Sutton, M., Rahman, I., & Garwood, R. (2014). Techniques for virtual palaeontology. John Wiley & Sons.

Tashman, S., & Anderst, W. (2003). In-vivo measurement of dynamic joint motion using high speed biplane radiography and CT: application to canine ACL deficiency. J. Biomech. Eng., 125(2), 238-245.

Taylor, M. P. (2014). Quantifying the effect of intervertebral cartilage on neutral posture in the necks of sauropod dinosaurs. PeerJ, 2, e712.

Taylor, M. P. (2022). Almost all known sauropod necks are incomplete and distorted. PeerJ, 10, e12810.

Taylor, M. P., & Wedel, M. J. (2013). The effect of intervertebral cartilage on neutral posture and range of motion in the necks of sauropod dinosaurs. PLoS One, 8(10), e78214.

Thompson, S., & Holmes, R. (2007). Forelimb stance and step cycle in *Chasmosaurus irvinensis* (Dinosauria: Neoceratopsia). Palaeontologia Electronica, 10(1), 1-17.

Troelsen, P.V., Wilkinson, D.M., Seddighi, M., Allanson, D.R. and Falkingham, P.L., 2019. Functional morphology and hydrodynamics of plesiosaur necks: does size matter?. Journal of Vertebrate Paleontology, 39(2), p.e1594850.

Tsai, H. P., & Holliday, C. M. (2015). Articular soft tissue anatomy of the archosaur hip joint: structural homology and functional implications. Journal of Morphology, 276(6), 601-630.

Tsai, H. P., Middleton, K. M., Hutchinson, J. R., & Holliday, C. M. (2018). Hip joint articular soft tissues of non-dinosaurian Dinosauromorpha and early Dinosauria: evolutionary and biomechanical implications for Saurischia. Journal of Vertebrate Paleontology, 38(1), e1427593.

Tsai, H. P., Turner, M. L., Manafzadeh, A. R., & Gatesy, S. M. (2019). Contrast-enhanced XROMM reveals in vivo soft tissue interactions in the hip of *Alligator mississippiensis*. Journal of anatomy.

Vidal, D., Mocho, P., Aberasturi, A., Sanz, J. L., & Ortega, F. (2020). High browsing skeletal adaptations in Spinophorosaurus reveal an evolutionary innovation in sauropod dinosaurs. Scientific reports, 10(1), 1-10.

Vidal, D., Mocho, P., Páramo, A., Sanz, J. L., & Ortega, F. (2020). Ontogenetic similarities between giraffe and sauropod neck osteological mobility. PLoS One, 15(1), e0227537.

von Huene, F. (1928). Lebensbild des Saurischier-Vorkommens im obersten Keuper von Trossingen in Württemberg. Haim.

von Sömmerring, S. T. (1817). Über einen Ornithocephalus brevirostris der Vorwelt.

Welles, S. P. (1984). *Dilophosaurus wetherilli* (Dinosauria, Theropoda). Osteology and comparisons. Palaeontographica Abteilung A, 85-180.

White, M. A., Bell, P. R., Cook, A. G., Barnes, D. G., Tischler, T. R., Bassam, B. J., & Elliott, D. A. (2015). Forearm range of motion in *Australovenator wintonensis* (Theropoda, Megaraptoridae). PloS one, 10(9), e0137709.

White, M. A., Cook, A. G., Klinkhamer, A. J., & Elliott, D. A. (2016). The pes of Australovenator wintonensis (Theropoda: Megaraptoridae): analysis of the pedal range of motion and biological restoration. PeerJ, 4, e2312.

Witmer, L. M., & Thomason, J. J. (1995). The extant phylogenetic bracket and the importance of reconstructing soft tissues in fossils. Functional morphology in vertebrate palaeontology, 1, 19-33.

Yalden, D. W. (1966). A contribution to the functional morphology of the mammalian carpus (Doctoral dissertation, University of London).

You, B. M., Siy, P., Anderst, W., & Tashman, S. (2001). In vivo measurement of 3-D skeletal kinematics from sequences of biplane radiographs: application to knee kinematics. IEEE transactions on medical imaging, 20(6), 514-525.

Zhang, R., Ji, Q., Luo, G., Xue, S., Ma, S., Li, J., & Ren, L. (2017). Phalangeal joints kinematics during ostrich (Struthio camelus) locomotion. *PeerJ*, *5*, e2857.

7 Appendix 1 – Data

The data for this project is available at the following links:

Chapter 2 (Calibration input files): https://doi.org/10.6084/m9.figshare.21534141

> Experimental setup files including calibration data, 3D model and images

Chapter 3 (Accuracy and Precision) Dataset: https://doi.org/10.6084/m9.figshare.21534153

> Dataset using LEGO wand to assess accuracy and precision at various camera settings (e.g. resolutions, framerates).

Chapter 4 (Ostrich Data): https://doi.org/10.6084/m9.figshare.21534531

> Dataset assessing effectiveness of setup on biological data through dissection of ostrich foot.

These are housed together in the following project:
https://figshare.com/projects/Quantifying_3D_range_of_motion_using_off-the-shelf_low-cost_cameras/153105